Master's thesis

NTNU
Norwegian University of Science and Technology
Faculty of Information Technology and Electrical Engineering
Department of Engineering Cybernetics

Henrik Adrian Hansen

Guidance for a fixed-wing UAV under large environmental forces

Master's thesis in Cybernetics and Robotics
Supervisor: Kristoffer Gryte
June 2023

NTNU
Norwegian University of
Science and Technology

Henrik Adrian Hansen

Guidance for a fixed-wing UAV under large environmental forces

Master's thesis in Cybernetics and Robotics
Supervisor: Kristoffer Gryte
June 2023

Norwegian University of Science and Technology
Faculty of Information Technology and Electrical Engineering
Department of Engineering Cybernetics

NTNU
Norwegian University of
Science and Technology

Abstract

This master's thesis investigates guidance laws for fixed-wing Unmanned Aerial Vehicles (UAVs). The research has importance for applications such as aerial surveys, remote sensing, and environmental monitoring, where UAVs often encounter large environmental forces. The main focus is the Line-of-sight (LOS) guidance law, applied to UAVs using the coordinated-turn relation.

Different variations of the coordinated-turn-inspired guidance law are tested in simulations with strong winds, turbulence, and gust. The guidance law was derived by considering non-zero Angle of Attack (AOA) and sideslip (SSA) to examine the underlying assumptions of the coordinated turn relationship, which were shown to be valid in most cases. The robustness of the guidance law was evaluated by adding bias to the AOA, SSA, pitch, and heading angle estimates. The simulation results indicated that incorporating additional estimates and aerodynamics into the guidance system did not significantly improve performance, as the estimates were mostly small and had little impact. Conversely, there was a potential risk of degrading performance due to inaccurate estimates. Nonetheless, the aircraft demonstrated the ability to follow the desired path with some bias.

A mathematical analysis is performed to explore the integral LOS inspired by coordinated turn. The analysis revealed uniform global asymptotic stability (UGAS) and uniform local exponential stability (ULES) properties, resulting in global κ-exponential stability. These techniques were further tested in simulations alongside other integral LOS variations. The results demonstrated that while they effectively eliminated steady-state errors, they also led to increased overshoot. The selection of the integral gain was considered crucial, particularly when the growth of the integral state was not appropriately scaled.

Ultimately, a comparison was made between the coordinated-turn-inspired LOS guidance laws and the popular state-of-the-art L1 guidance law. The performance of these approaches was found to be quite similar, with only slightly more overshoot observed in certain situations for the L1 guidance law. However, the L1 guidance law was deemed a more robust choice as it relies on fewer estimates.

Sammendrag

Denne masteroppgaven undersøker styrelover for fastvingede ubemannede luftfartøy (UAVer). Forskningen har betydning for bruksområder som flyfotografering, fjernmåling og miljøovervåking, hvor UAVer ofte møter store ytre påvirkninger. Hovedfokuset er synslinjestyreloven (LOS), anvendt på UAVer ved bruk av den koordinerte svingrelasjonen.

Forskjellige varianter av styreloven inspirert av koordinert sving blir testet gjennom simuleringer med kraftig vind, turbulens og vindkast. Styreloven ble utledet med ikke-null angrepsvinkel (AOA) og sideslipvinkel (SSA) for å undersøke de underliggende antakelsene i den koordinerte svingrelasjonen, som viste seg å være gyldig i de fleste tilfeller. Robustheten til styreloven ble vurdert basert på avvik i AOA, SSA, helning og heading. Simuleringsresultatene indikerte at inkludering av flere estimater og aerodynamikk i styresystemet ikke forbedret ytelsen vesentlig, siden estimatene var for det meste små og påvirket ikke ytelsen nevneverdig. Tvert imot var det en potensiell risiko for forringelse av ytelsen på grunn av unøyaktige estimater. Likevel viste flyet evnen til å følge den ønskede banen med noe avvik.

En matematisk analyse ble utført for å utforske integrale synslinjemetoder inspirert av koordinerte svinger. Analysen avslørte uniform global asymptotisk stabilitet (UGAS) og uniform lokal eksponensiell stabilitet (ULES), noe som resulterer i global κ-eksponentiell stabilitet. Disse teknikkene ble videre testet gjennom simuleringer sammen med andre integrale synslinjevarianter. Resultatene viste at de effektivt eliminerte steady-state-feil, men førte også til økt overskytelse. Valget av integrale forsterkningen ble ansett som avgjørende, spesielt når veksten i integraltilstanden ikke var skalert.

Til slutt ble det foretatt en sammenligning mellom styreloven inspirert av koordinerte svinger og den populære L1 styreloven. Ytelsen til disse styrelovene viste seg å være ganske lik, med bare noe mer overskytelse observert i visse situasjoner for L1-styreloven. Imidlertid ble L1 ansett som et mer robust valg, da den er avhengig av færre estimater.

Preface

This report is the result of my master's thesis completing a 5-year study in Cybernetics and Robotics at the Department of Engineering Cybernetics at the Norwegian University of Science and Technology (NTNU). It continues the work of the project thesis with the same title [1], building on Chapter 10 in the doctor thesis of Kristoffer Gryte [2]. It investigates the performance coordinated-turn-inspired LOS guidance for UAVs and contributes by adding integral action.

I would like to thank Kristoffer Gryte and Tor Arne Johansen for supervising and guiding me through the research. You have provided valuable insight and feedback in addition to laying the foundations of my work. I would also like to thank the developers who contribute to and maintain the open-source projects I have been using: JSBSim and Ardupilot. Ultimately, I want to thank my friends and family for their love and support throughout the course of this work.

Abbrevations

UAV Unmanned aerial vehicle

LOS Line of sight

SITL Software in the loop

AHRS Attitude and heading reference system

TECS Total energy control system

EKF Extended Kalman Filter

GNSS Global navigation satellite systems

AGL Above ground level

FPA Flight Path Angle

AOA Angle of attack

SSA Sideslip angle

WP Waypoint

LFC Lyapunov function candidate

UGAS Uniformly globally asymptotically stable

ULES Uniformly locally exponentially stable

USGES Uniformly semiglobal exponentially stable

Contents

Chapter 1

Introduction

Unmanned Aerial Vehicles (UAVs) have gained widespread attention in recent years due to their potential for various applications, such as search and rescue, surveillance, and monitoring. Norway has vast, remote areas that contain economically critical marine resources like fishery, petroleum, and in the near future, offshore wind. Monitoring in these areas can be dangerous, time-consuming, or unfeasible for human pilots. UAVs can automate these tasks and other interesting applications like delivering packages [3]. Furthermore, UAVs offer several advantages over traditional human-crewed aircraft, including lower costs and increased flexibility without risk to human pilots.

However, UAVs face several challenges that make their operations more complex, particularly in conditions with large environmental forces. The Norwegian Sea and coastline are known for severe and unpredictable weather. The impact of atmospheric disturbances on UAVs can cause deviations in their flight path, leading to accidents or mission failures. This challenge makes it essential to develop guidance systems that effectively steer UAVs in these environments and ensure their safe and successful operation.

Guidance determines the appropriate control inputs to guide a UAV along a desired trajectory. This thesis deals with the lateral path-following problem, where a path is pursued without temporal constraints. A substantial amount of research has been done on LOS guidance for marine vehicles [4],[5],[6]. It is a popular and simple guidance scheme for marine vehicles, imitating a steersman at the helm, but originating from the missile community [7]. It has been adopted for fixed-wing UAVs in [2]. Fixed-wing UAVs do not follow LOS heading/course references directly; fixed-wing aircraft turn by rolling. The commands must therefore be translated to roll using aerodynamics. This requires more state estimation and assumptions. The validity of these assumptions is interesting to take a closer look at. The robustness of the guidance law is also an important aspect. How biased can

the estimates in the guidance law be before the states are not worth estimating? This is especially interesting for the heading angle, which is usually measured by a magnetometer - known to be unreliable.

For combating constant or slowly varying disturbances, adding integral action to the LOS guidance law can be helpful. This had been done effectively for marine vessels [8] [9], but not to the same extent for UAVs. An alternative is adaptive LOS explored in [10]. For more time-varying disturbances, for which integral or adaptive LOS fall short, extended-state observer LOS is better suited [11]. It is implemented in [12] and [13]. A more popular guidance scheme for UAVs is L1 guidance, introduced in [14] and further developed in [15] and [16]. It is the guidance method used in Ardupilot and PX4, which are popular autopilot software libraries.

The purpose of this master thesis is to investigate further guidance for fixed-wing UAVs that can operate effectively under large environmental forces, particularly atmospheric disturbances. The contributions are: Further evaluating the effectiveness of coordinated-turn LOS guidance building on [2] and [1] in SITL simulations with complexity beyond [2] by variations in flight path angle, bias in estimates, and other atmospheric disturbances like gusts and turbulence. The simulation results are used to comment on the robustness of the guidance law. Furthermore, the validity of the coordinated turn assumptions is inspected by comparing different variants of coordinated turn LOS, most importantly assuming AOA and SSA to be zero. In this respect, another addition is deriving the coordinated turn LOS with non-zero AOA and SSA. Moreover, integral action will be added to coordinated-turn LOS building on [8]. The new contribution is adopting cross-track error integral LOS to fixed-wing UAVs by coordinated turn and a stability proof for global k-exponential stability for a simpler, more general version of the guidance law. Integral coordinated-turn LOS is compared to cross-track error integral LOS in simulations, inspired by the same guidance principle introduced in [8]. Ultimately the performance of the coordinated-turn LOS guidance law will be compared to the L1 guidance scheme. This has been done extensively in [2], but in this thesis, the comparison is done with and without integral action to evaluate how integral coordinated-turn LOS compares to the obvious alternative integral L1 guidance.

Chapter 2

Theory

This chapter summarizes the relevant theoretical background necessary for the later chapters. Section 2.1 and Section 2.2 is, with a few exceptions, taken from [1] as the definitions and relations for aerodynamics and guidance are the same. A notable exception is Section 2.1.2, introducing the coordinated turn relation, which is heavily inspired by Chapter 7 in [2]. Section 2.3 is a summary of integral LOS guidance literature. Section 2.4 explores coordinated-turn-inspired LOS. The derivation in Section 2.4 is inspired by Chapter 10 in [2], while Section 2.4.2 is a new contribution containing mathematical analysis and a stability proof for integral coordinated-turn-inspired LOS building on [8].

2.1 Aerodynamics

2.1.1 Fixed-wing aircraft dynamics

The following subchapter summarizes necessary fixed-wing aircraft dynamics described in [17].

Consider the coordinate frames below for expressing position, orientation, and other important quantities.

1. The North-East-Down (NED) coordinate frame is an inertial, earth-fixed coordinate system denoted by {n}. Its origin is at a defined home location; the x-axis is pointed north, the y-axis east, and the z-axis down.
2. The body frame denoted by {b}. The origin is centered in the vehicle, and the axes follow the FRD convention: the x-axis pointing forward, the y-axis right, and the z-axis down by the right-hand rule.
3. The ground velocity frame {v}, which is a NED frame centered in the aircraft with the x-axis aligned with the ground velocity vector $\mathbf{V}_g$. This is achieved by rotating NED by the course angle χ around the z-axis and FPA γ around

the y-axis.

4. The wind frame {w} whose origin is also centered in the vehicle, where the x-axis is aligned with the air velocity vector, the y-axis is rotated by air relative bank angle μ_a, and z is determined by the right-hand rule.
5. The path-tangential coordinate frame {p}, where the origin is located in $\mathbf{p}_k^n$ and the axes are rotated an angle χ_p relative to {n} around the z-axis such that the x-axis is pointed toward $\mathbf{p}_{k+1}^n$

Aircraft with GNSS can measure position $\mathbf{p}_{nb}^n \in \mathbb{R}^3$ and linear velocity $\mathbf{v}_{nb}^n \in \mathbb{R}^3$ in the NED frame. It is useful to express them in the body frame by

$$\mathbf{v}_{nb}^b = \mathbf{R}_n^b(\phi, \theta, \psi)\mathbf{v}_{nb}^n = \begin{bmatrix} u \\ v \\ w \end{bmatrix} \tag{2.1}$$

where $\mathbf{R}_n^b(\phi, \theta, \psi)$ is the rotation matrix from {n} to {b}, which can be defined by the Euler angles roll, pitch, and yaw. The yaw angle ψ is also called heading.

The derivatives of the Euler angles can be expressed by the body-frame angular rates, p, q, and r as

$$\begin{bmatrix} \dot{\phi} \\ \dot{\theta} \\ \dot{\psi} \end{bmatrix} = \begin{bmatrix} 1 & \sin\phi\tan\theta & \cos\phi\tan\theta \\ 0 & \cos\phi & -\sin\phi \\ 0 & \sin\phi\sec\theta & \cos\phi\sec\theta \end{bmatrix} \begin{bmatrix} p \\ q \\ r \end{bmatrix} \tag{2.2}$$

The linear velocity in the body frame is often denoted as ground velocity $\mathbf{V}_g$, while the ground speed $V_g = ||\mathbf{V}_g|| = \sqrt{u^2 + v^2 + w^2}$. The angle between the horizontal component of the ground velocity and the x-axis of {n} is named course denoted χ. The angle between the ground velocity vector and it's horizontal components is called the flight path angle, γ. Together they describe the ground velocity vector's direction in relation to the inertial frame {n}. The aircraft's velocity in relation to the surrounding air is named the airspeed vector $\mathbf{V}_a$. It is related to the ground speed vector by the wind speed $\mathbf{V}_w$ by

$$\mathbf{V}_a = \mathbf{V}_g - \mathbf{V}_w \tag{2.3}$$

Equation (2.3) is often referred to as the "wind triangle" and is displayed in Figure 2.1 and Figure 2.2. In the same manner as the ground velocity vector, the airspeed vector is related to the inertial frame by the air-relative course angle χ_a and the air-relative flight path angle γ_a. The difference between course and heading is called the crab angle χ_c

$$\chi_c = \chi - \psi \tag{2.4}$$

The crab angle is non-zero during turns and/or in the presence of a disturbance like the wind. The heading angle can be estimated using measurements from magnetometers and digital compasses. In practice, obtaining an accurate estimate can be difficult because the sensors are sensitive to electromagnetic interference from electric motors, servos, and wiring. Careful sensor placement can reduce this, but some bias should be expected. The course angle can be estimated using GNSS velocity measurements' north and east components. With knowledge of the ground speed vector's horizontal component V_d, one can find an expression for the flight path angle.

$$\chi = \text{atan}(\frac{V_n}{V_e}), \quad \gamma = \text{atan}(-\frac{V_d}{V_g}) \tag{2.5}$$

Typically, the uncertainty of the GNSS measurements is lower than that of the magnetometer measurements. However, the uncertainty of the course estimate will increase as the ground speed decreases. This is reasonable as ground speed is not defined for a stationary craft. The heading angle, on the other hand, is always defined.

Angle of attack α and sideslip angle β are defined as

$$\begin{aligned} \alpha &= \text{atan}(\frac{w_r}{u_r}) \\ \beta &= \text{atan}(\frac{v_r}{V_a}) \end{aligned} \tag{2.6}$$

2.1.2 Coordinated turn

It is beneficial for fixed-wing aircraft to "carve" turns instead of skidding or using the rudder. This is achieved during the coordinated turn flight condition. This subsection will derive the coordinated turn equation with the same approach as chapter 7 in [2] with the exception of assuming $\alpha = \beta = 0$. The reason behind this is to be able to test the validity of the assumption. Furthermore, the assumption can always be reintroduced later to arrive at the same result as [2].

The following assumptions are made in the coordinated turn relation:

A1 The lift force works along the negative z-component of the wind frame that cancels out the force of gravity in the inertial frame. The dynamics of the lift force are neglected.

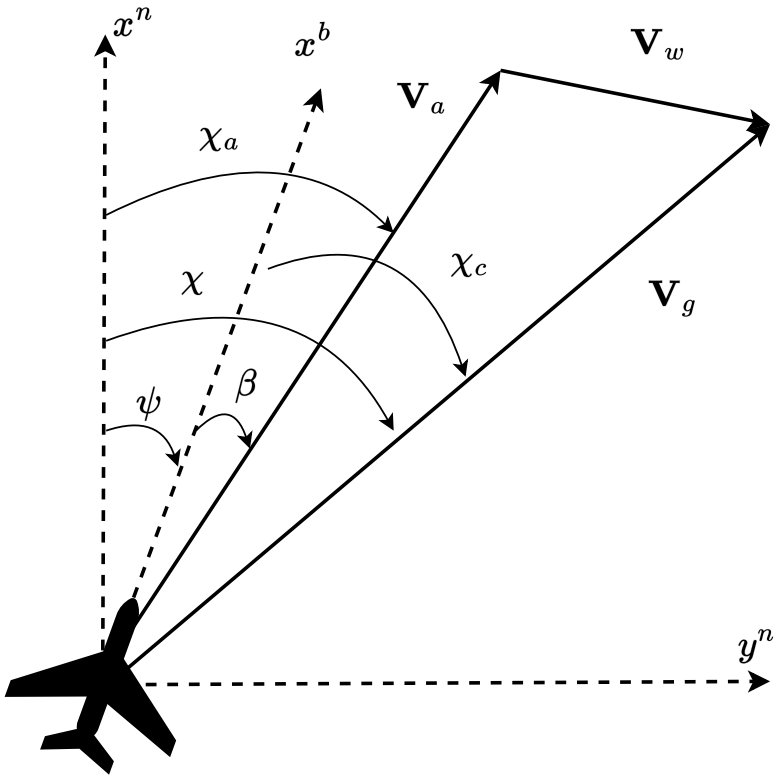

Figure 2.1: Wind triangle in the horizontal plane, inspired by Figure 2.10 in [17] assuming horizontal airspeed such that $\chi_a = \psi + \beta$

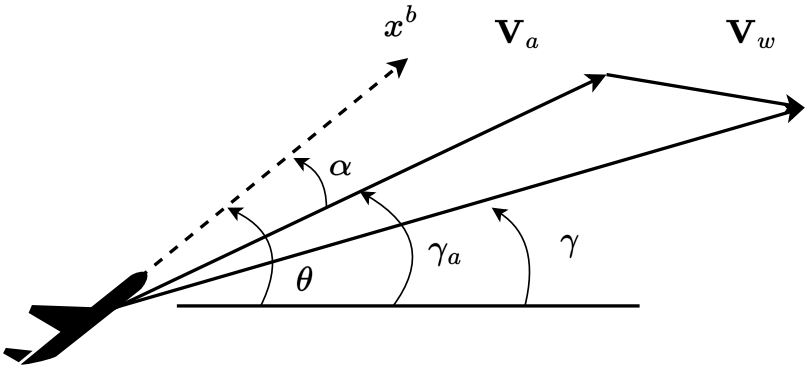

Figure 2.2: Wind triangle in the vertical plane, inspired by Figure 2.12 in [17] assuming wings-level-flight such that $\gamma_a = \theta - \alpha$

A2 The drag force holds no significance when compared to the lift force and is therefore not considered.
A3 All linear velocity is tangential to the arc, such that the centripetal acceleration can be expressed by $a = v\omega$.
A4 The air-relative course angle can be approximated by $\chi_a = \psi + \beta$
A5 The air-relative flight path angle γ_a, can be approximated by $\gamma_a = \theta - \alpha$

Note that the approximations A4 and A5 ([18], eq 2.2-38,39), come from other assumptions that are not necessarily true. A4 assumes wings-level flight, and A5 requires horizontal airspeed.

As $\alpha = \beta = 0$ is a common assumption, that will be a focus of this thesis, it will from here on be referred to as Assumption 6 (A6).

With Assumptions A1-A5, the following force balance can be set up in the horizontal projection of the ground velocity frame, denoted {t} where the lift force counterbalances the centripetal acceleration and the gravitational force.

$$\mathbf{F}_l^t = \mathbf{R}_{tw} \begin{bmatrix} 0 \\ 0 \\ -f_L \end{bmatrix} = m\vec{a} = \begin{bmatrix} 0 \\ mv\omega \\ mg \end{bmatrix} \begin{bmatrix} 0 \\ mV_g \cos(\gamma)\dot{\chi} \\ mg \end{bmatrix} \tag{2.7}$$

where the rotation matrix is given by

$$\mathbf{R}_{tw} = \mathbf{R}_z(\chi - \chi_a)\mathbf{R}_y(-\gamma_a)\mathbf{R}_x(-\mu_a) \tag{2.8}$$

The coordinated turn relation can be extracted from the force balance by the division of the y-component by the z-component of Equation (2.7).

$$\frac{\cos(\beta - \chi + \psi)\sin(\mu_a) + \sin(\alpha - \theta)\sin(\beta - \chi + \psi)\cos(\mu_a)}{\cos(\mu_a)\cos(\alpha - \theta)} = \frac{V_g \cos(\gamma)\dot{\chi}}{g} \tag{2.9}$$

An expression for the time derivative of the course angle can be found by solving for $\dot{\chi}$

$$\dot{\chi} = \frac{g\cos(\beta - \chi + \psi)}{V_g \cos(\gamma)\cos(\alpha - \theta)}(\tan(\mu_a) + \sin(\alpha - \theta)\tan(\beta - \chi + \psi)) \tag{2.10}$$

Equation (2.9) can also be used to express the bank angle μ_a. It is desirable to translate it to the roll angle which can be used as a reference signal in an attitude

controller. From [2] bank and roll have the following relation when the wind is not considered:

$$\mu_a = \text{acos}(\frac{\sin(\alpha)\sin(\theta) + \cos(\alpha)\cos(\phi)\cos(\theta)}{\cos(\alpha - \theta)}) \tag{2.11}$$

solving for ϕ results in

$$\phi = \text{acos}(\frac{\cos(\mu_a)\cos(\alpha - \theta) - \sin(\alpha)\sin(\theta)}{\cos(\alpha)\cos(\theta)}) \tag{2.12}$$

By assuming $\beta = \gamma = \alpha - \theta = 0$, which implies $\mu_a = \phi$, Equation (2.10) can be simplified to

$$\dot{\chi} = \frac{g}{V_g} \tan\phi \cos(\chi - \psi), \tag{2.13}$$

2.1.3 Trim conditions

An aircraft is said to be in trim conditions when it is traveling at a constant speed V_g^*, climbing at a constant flight path angle γ^*, and is in a constant orbit of radius R^*. It is considered an equilibrium for the aircraft. If the wind is treated as an unknown disturbance and assumed zero, the heading rate in trim conditions can be expressed as [17]

$$\dot{\psi}^* = \frac{V_g^*}{R^*} \cos\gamma^* \tag{2.14}$$

For an aircraft in trim conditions flying at a constant altitude ($\gamma = 0$), combining Equation (2.13) and Equation (2.14) gives a relation between the centripetal acceleration of the orbit and the roll angle by

$$a = \frac{V_g^2}{R} = \text{atan}(\phi)g \tag{2.15}$$

2.2 Guidance

2.2.1 LOS

Line-of-sight (LOS) guidance can be used to follow a straight line connecting two consecutive waypoints, WP_k and WP_{k+1} by computing a course reference

for the autopilot. By the definition in [19], the along-path and cross-track errors are defined in {p} by

$$\begin{bmatrix} x_e \\ y_e \end{bmatrix} = \mathbf{R}_p^n(\chi_p)^\intercal \begin{bmatrix} x - x_k \\ y - y_k \end{bmatrix} \tag{2.16}$$

where (x, y) and (x_k, y_k) are the vehicle position and the previous waypoint defined in {n}. The rotation matrix defining the rotation from {p} to {n} is defined by

$$\mathbf{R}_p^n(\chi_p) = \begin{bmatrix} \cos(\chi_p) & -\sin(\chi_p) \\ \sin(\chi_p) & \cos(\chi_p) \end{bmatrix} \tag{2.17}$$

where χ_d is the path-tangential angle

$$\chi_p = \operatorname{atan2}(y_{k+1} - y_k, x_{k+1} - x_k) \tag{2.18}$$

The objective is to minimize the cross-track error y_e [4] such that

$$\lim_{t \to \infty} y_e(t) = 0. \tag{2.19}$$

From Equation (2.17) and Equation (2.18) the cross-track error can be expressed as

$$y_e = -(x - x_k)\sin(\chi_p) + (y - y_k)\cos(\chi_p) \tag{2.20}$$

The LOS guidance law steers the aircraft along a LOS vector drawn from the craft towards a point on the desired path, defined by a look-ahead distance Δ from where the aircraft was supposed to be on the path. The principle is illustrated in Figure 2.3.

The LOS guidance law gives the desired course by [9]

$$\chi_d = \operatorname{atan}(\frac{-y_e}{\Delta}) + \chi_p \tag{2.21}$$

It is desirable to express look-ahead distance dependent on ground speed and look-ahead time to give similar performance in the presence of head and tail wind. This can be achieved by:

$$\Delta = \Delta_t V_g \tag{2.22}$$

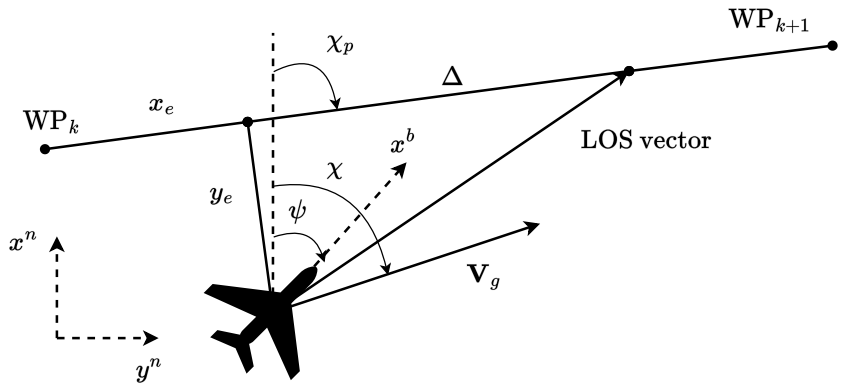

Figure 2.3: LOS principle, inspired by Figure 1 in [4]

where Δ_t is a design parameter.

As stated in Section 2.1.1, it is desirable for fixed-wing UAVs to "carve" turns in the coordinated flight condition. To achieve this the controller needs a roll command from the guidance system. The course reference from Equation (2.21) can be transformed into a roll reference by the coordinated turn equation. However, the derivative of the desired course is needed. It is given by time differentiation of Equation (2.21)

$$\dot{\chi}_d = -\frac{\Delta}{\Delta^2 + y_e^2}\dot{y}_e + \dot{\chi}_p \tag{2.23}$$

For a series of waypoints connected by straight line segments, the derivative of the path-tangential angle is zero except for when the waypoint changes.

Time differentiation of y_e gives

$$\dot{y}_e = V_g \sin(\chi - \chi_p). \tag{2.24}$$

If perfect course angle tracking is assumed ($\chi = \chi_d$), Equation (2.21) renders the equilibrium $y_e = 0$ of Equation (2.24) USGES [20]. USGES is a form of stability slightly weaker than global exponential stability but with nice robustness properties. However, it is stronger than global κ-exponential stability as defined in [21]. Global κ-exponential stability is equivalent to the combination of UGAS and ULES [22].

2.2.2 L1

L1 guidance generates a lateral acceleration command based on the angle between the vehicle's velocity vector and a vector from the vehicle to a reference point on the trajectory [14]. The reference point is chosen a constant L1 distance ahead of the vehicle. The principle is illustrated in Figure 2.4. The lateral command is given by

$$a_{cmd} = 2\frac{V_g^2}{L_1}\sin\eta \tag{2.25}$$

As stated in [15], the acceleration command will be equal to the centripetal acceleration needed to follow a circle passing through both the vehicle and the reference point at a constant speed with the vehicle velocity vector as a tangent. This can be seen from Equation (2.25) with $a_{cmd} = \frac{V_g^2}{R}$ and $R = \frac{L_1}{2\sin\eta}$.

For a fixed-wing attitude controller, the acceleration reference needs to be converted into a roll command by assuming trim conditions with Equation (2.15) giving

$$\phi_{cmd} = \text{atan}\,\frac{a_{cmd}}{g} \tag{2.26}$$

To find η, one can split the angle into η_1 and η_2 as shown in Figure 2.4 [16]. By inspection

$$\eta_1 = \text{asin}(\frac{y_e}{L1}), \quad \eta_2 = \text{atan}(\frac{V_{ye}}{V_{xe}}) \tag{2.27}$$

where V_{ye} and V_{xe} is the projected groundspeed cross-track and along-track the path. As with lookahead distance, L_1 distance can also be expressed dependent on V_g.

$$L_1 = V_g T \tag{2.28}$$

where T is the L_1 ratio.

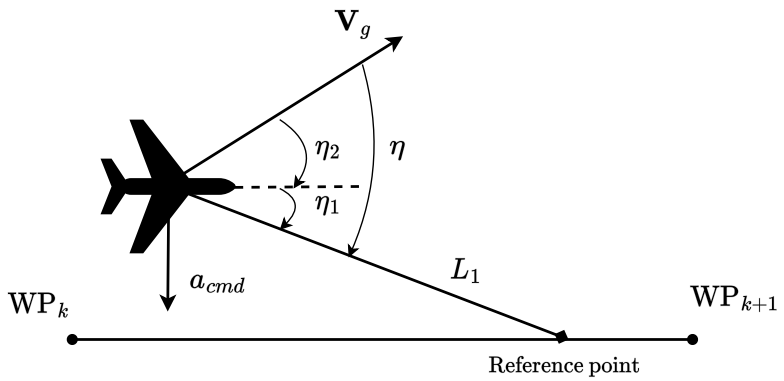

Figure 2.4: L1 principle, inspired by Figure 3 in [15]. Note that η is chosen larger than necessary for showing $\mathbf{V}_g$ as a tangent to the aircraft's arc in favor of displaying the difference of η_1 and η_2

.

2.3 Integral guidance

2.3.1 Integral LOS

In addition to being simple and intuitive, LOS guidance is vulnerable to environmental disturbances, like the wind. It can not be overcome by adding integral effect in the angle controller because the problem originates in the reference signal from the guidance system. The integral effect must therefore be added to the guidance law to ensure path convergence. Several variants exist.

Control law comparison

An intuitive but naive way to add integral effect to LOS guidance is to view Equation (2.21) as a saturated proportional control law and expand it with an integral term as proposed in [23]. It then takes the form of a PI-controller whose output is mapped to $(\frac{-\pi}{2} + \chi_p, \frac{\pi}{2} + \chi_p)$

$$\chi_d = \text{atan}(-K_p y_e(t) - K_i \int_0^t y_e(\tau) d\tau) + \chi_p \tag{2.29}$$

where $K_p = \frac{1}{\Delta}$. The same principle is used with proportional navigation for ballistic missiles in [24]. A drawback of this solution is that the integral term can grow very large when the vehicle is far away from the desired path.

One way to counter this is to substitute temporal integration with spatial integration as done in [25]. For straight-line path following:

$$\chi_d = \text{atan}(-K_p y_e(t) - K_i \int_0^l y_e(l)dl) + \chi_p \tag{2.30}$$

where l is the progress along the desired path. This reduces the risk of overshoot and anti-windup by not blowing up the integral state when the velocity vector does not have a component along the desired path. [25] expands this beyond straight lines to include arcs as well. Note that l is a time-dependent function of the dynamics of the vehicle, making it possible to express the integral in Equation (2.30) as

$$\int_0^l y_e(l)dl = \int_0^t y_e(\tau)\frac{dl}{d\tau}d\tau \tag{2.31}$$

where $\frac{dl}{dt}$ is the vehicle's velocity projected unto the desired path.

[23] also suggests adding a damping term to the "PI" controller structure to reduce overshoot.

Another alternative is to add an integral state dependent on cross-track error, first introduced in [8]. The guidance law can be stated as

$$\begin{aligned} \psi_d &= \text{atan}(\frac{-(y_e + \sigma y_{int})}{\Delta}) + \chi_p - \chi_c \\ \dot{y}_{int} &= \frac{\Delta y_e}{(y_e + \sigma y_{int})^2 + \Delta^2} \end{aligned} \tag{2.32}$$

where the integral gain σ is a design parameter. A nice property of this guidance law is that the rate of integration $\dot{y}_{int} \to 0$ as $y_e \to \infty$, lowering the risk of integrator-windup as the rate of integration slows down for large cross-track errors. Note that the guidance law gives a heading reference. No side-slip estimate is included in the guidance law because the integral term will account for it when the vehicle is on the desired path.

It is extended to three dimensions for AUVS in [26] and used on snake robots in [27]. It has also been used to automatically control sailboats by using the integral LOS law in three different control modes depending on sailing "modes" [28].

The same idea can be used for giving a course reference signal, as done in [9]. Here the integral state is made dependent on speed U where the derivative of the integral state is given as

$$\dot{y}_{int} = \frac{U y_e}{\sqrt{(y_e + \sigma y_{int})^2 + \Delta^2}} \tag{2.33}$$

Note that the square root in the denominator will remove the anti-wind-up effect intended by Equation (2.32)

Other versions of integral LOS

A modified integral LOS guidance law is proposed in [29] where the derivative of the integral state is also dependent on the cross-track error rate.

A similar version is proposed in [30] where a heading reference is computed by

$$\begin{aligned} \phi_d &= \chi_p - \beta - \arctan(k_{p1} y_e) - y_{int} \\ \dot{y}_{int} &= \frac{k_{p2} y_e}{\sqrt{1 + (k_{p2} y_e)^2}} (1 - \frac{\lambda}{Q} \dot{y}_e), \quad \lambda = \begin{cases} -1, & \dot{y}_e < 0 \\ 1, & \dot{y}_e \geq 0 \end{cases} \end{aligned} \tag{2.34}$$

where the constants $k_{p1,2}$ and Q are design parameters.

2.3.2 L1 integral effect in Ardupilot

Ardupilot employs the L1 guidance method [15] with integral effect. An integral state is added to $\eta_1 = \arcsin(\frac{y_e}{L_1})$ and computed in discrete time as

$$\eta_{int_i} = \eta_{int_{i-1}} + \sigma \eta_1 dt \tag{2.35}$$

where σ is the integral gain and dt is the time since the last iteration. Integral wind-up is avoided by not growing the integral state when $\eta_1 > 5$ rad and constraining the integral state to $[-0.1, 0.1]$.

2.4 Coordinated-turn-inspired LOS

This section derives coordinated-turn-inspired LOS and adds integral action to the control law.

2.4.1 Derivation with non-zero AOA and SSB

As LOS guidance law in Equation (2.21) guarantees $y_e \to 0$ under perfect course tracking, [20], the next step is finding a controller tracking desired course. This section will follow the procedure in Chapter 10 of [2], which is replicated in [1], without Assumption A6.

One can ensure that $\chi \to \chi_d$ by inspecting the LFC $V = \frac{1}{2}\tilde{\chi}^2$ dependent on the error variable $\tilde{\chi} = \chi_d - \chi$. The time derivative of V is

$$\dot{V} = \tilde{\chi}\dot{\tilde{\chi}} = \tilde{\chi}(\dot{\chi}_d - \dot{\chi}) \tag{2.36}$$

where $\dot{\chi}$ is given by Equation (2.10), χ_d by Equation (2.21), $\dot{\chi}_d$ by Equation (2.23) and $\dot{y}_e$ by Equation (2.24). Inserting Equation (2.10) gives

$$\dot{V} = \tilde{\chi}(\dot{\chi}_d - \frac{g\cos(\beta - \chi + \psi)}{V_g \cos(\gamma)\cos(\alpha - \theta)}(\tan(\mu_a) + \sin(\alpha - \theta)\tan(\beta - \chi + \psi))) \tag{2.37}$$

Observe that the course error dynamics are nonautonomous. Assuming perfectly tracked bank angle such that $\mu_a = \mu_{a,d}$ and choosing

$$\mu_{a,d} = \text{atan}(\frac{V_g \cos(\gamma)\cos(\alpha - \theta)}{g\cos(\beta - \chi + \psi)}(f(\tilde{\chi}) + \dot{\chi}_d) - \sin(\alpha - \theta)\tan(\beta - \chi + \psi)) \tag{2.38}$$

[2]

where $f(\tilde{\chi})$ is an odd function, renders the equilibrium $\tilde{\chi} = 0$ UGAS by satisfying Theorem 4.9 in [31] as $\dot{V}$ is upper bounded by $\dot{V} = -W(\tilde{\chi}) < 0$ with positive definite $W(\tilde{\chi}) = f(\tilde{\chi})\tilde{\chi} > 0$. Note that choosing $f(\tilde{\chi})$ as an odd polynomial with positive coefficients will render the equilibrium UGES by Theorem 4.10 in [31] as $\dot{V} = -W(\tilde{\chi}) < ||\tilde{\chi}||^a$ for a positive constant a.

The desired bank angle can simply be translated to the desired roll by Equation (2.12) for the attitude controller.

With Assumption A6, $\alpha = \beta = 0$, it can be seen from Equation (2.12) that $\phi = \mu_a$, resulting in the coordinated turn LOS law from [2] by

$$\phi_d = \text{atan}(\frac{V_g \cos(\gamma)\cos(\theta)}{g\cos(\chi - \psi)}(f(\tilde{\chi}) + \dot{\chi}_d) - \sin(\theta)\tan(\chi - \psi)) \tag{2.39}$$

The interconnected system compromised of Equation (2.21) and Equation (2.39) has been shown to render the cross-track error, and the course error dynamics USGES in [2].

2.4.2 Coordinated-turn-inspired LOS with integral effect

Integral effect can be added to guidance in several ways, as explored in Section 2.3. In this section some of the aforementioned methods will be applied to coordinated-turn LOS described in Equation (2.39). Note that the main assumption in the derivation of the course controller in Section 2.4.1 is $\tilde{\chi} \to 0 \implies y_e \to 0$. Therefore the same approach can be used with other LOS guidance laws as long as they render the cross-track error dynamics asymptotically stable.

Cross-track error integral effect

In this section integral effect will be added to LOS guidance law in Equation (2.21) through the integral state defined in Equation (2.32) from [8]. Inspired by the proof in the same paper, it will be shown to guarantee the control objective in Equation (2.19).

Substituting the time integral in Equation (2.29) with an integral state gives

$$\chi_d = \text{atan}(-K_p y_e - K_i y_{int}) + \chi_p \tag{2.40}$$

Imitating LOS, the gains are chosen to be $K_p = 1/\Delta$ and $K_i = \sigma/\Delta$, where Δ is the lookahead distance and σ is integral gain.

By adding the definition of the integral state from Equation (2.32) to Equation (2.40) the guidance law is found to be

$$\begin{aligned} \chi_d &= \text{atan}(-K_p y_e - K_i y_{int}) + \chi_p \\ \dot{y}_{int} &= \frac{\Delta y_e}{\Delta^2 + (y_e + \sigma y_{int})^2} \end{aligned} \tag{2.41}$$

The cross-track error dynamics is found by inserting $\chi = \chi_d - \tilde{\chi}$ into Equation (2.24)

$$\dot{y}_e = V_g \sin(\chi_d - \tilde{\chi} - \chi_p) = -V_g \sin(\text{atan}(\frac{1}{\Delta} y_e + \frac{\sigma}{\Delta} y_{int}) + \tilde{\chi}) \tag{2.42}$$

Exploting $\sin(u+v) = \sin(u)\cos(v) + \cos(u)\sin(v)$

$$\dot{y}_e = -V_g \sin(\text{atan}(\frac{1}{\Delta} y_e + \frac{\sigma}{\Delta} y_{int}))\cos(\tilde{\chi}) - V_g \cos(\text{atan}(\frac{1}{\Delta} y_e + \frac{\sigma}{\Delta} y_{int}))\sin(\tilde{\chi}) \tag{2.43}$$

Using $\sin(\arctan(x)) = x/\sqrt{1+x^2}$ and $\cos(\arctan(x)) = 1/\sqrt{1+x^2}$ results in

$$\dot{y}_e = -V_g \frac{\Delta y_e + \sigma \Delta y_{int}}{\Delta^2 + (y_e + \sigma y_{int})^2} \cos(\tilde{\chi}) - V_g \frac{\Delta^2}{\Delta^2 + (y_e + \sigma y_{int})^2} \sin(\tilde{\chi}) \tag{2.44}$$

$$= -V_g \frac{(\Delta y_e + \sigma \Delta y_{int}) \cos(\tilde{\chi}) + \Delta^2 \sin(\tilde{\chi})}{\Delta^2 + (y_e + \sigma y_{int})^2} \tag{2.45}$$

Adding the definition of the integral state makes the full error dynamics

$$\begin{aligned} \dot{y}_e &= -V_g \frac{(\Delta y_e + \sigma \Delta y_{int}) \cos(\tilde{\chi}) + \Delta^2 \sin(\tilde{\chi})}{\Delta^2 + (y_e + \sigma y_{int})^2} \\ \dot{y}_{int} &= \frac{\Delta y_e}{\Delta^2 + (y_e + \sigma y_{int})^2} \end{aligned} \tag{2.46}$$

It is trivial to verify that the equilibrium of the system is $y_e = 0, \quad y_{int} = -\frac{\Delta}{\sigma} \tan(\tilde{\chi}) = y_{int}^{eq}$. Note that y_{int}^{eq} is not defined for $\tilde{\chi} = \frac{\pi}{2} + \pi k$ rad, where $k \in \mathbb{Z}$. Therefore stability can only be investigated inside the ball $\mathcal{B}_1\{\tilde{\chi} < \frac{\pi}{2} \text{ rad}\}$, which necessitates the following assumptions:

A7 The magnitude of the course error $\tilde{\chi}$ is less than $\pi/2$ rad
A8 The time derivative of y_{int}^{eq} is zero

It can be observed that V_g, and by extension Δ, are time-varying. This makes the system in Equation (2.46) nonautonomous.

Theorem 1. *Under Assumptions A7-A8, the integral LOS guidance law in Equation* (2.41) *applied to cross-track error dynamics in Equation* (2.46) *renders the equilibrium point* $(\dot{y}_e, \dot{y}_{int}^{eq}) = (0, 0)$ *globally* κ*-exponentially stable assuming look-ahead distance, ground speed and integral gain satisfy the conditions:*
$0 < \Delta \leq \Delta_{max}$, $0 < V_{g,min} \leq V_g \leq V_{g,max}$ *and* $0 < \sigma \leq V_{g,min}$

Proof. Consider the transformed system

$$\begin{aligned} z_1 &= y_{int} - y_{int}^{eq} \\ z_2 &= y_e + \sigma z_1 \end{aligned} \tag{2.47}$$

with time derivatives

$$\begin{aligned}\dot{z}_1 &= \frac{\Delta(z_2-\sigma z_1)}{\Delta^2+(z_2+\sigma y_{int}^{eq})^2}\\ \dot{z}_2 &= -V_g\frac{\Delta(z_2+\sigma y_{int}^{eq})\cos(\tilde{\chi})+\Delta^2\sin(\tilde{\chi})}{\Delta^2+(z_2+\sigma y_{int}^{eq})^2}+\sigma\frac{\Delta(z_2-\sigma z_1)}{\Delta^2+(z_2+\sigma y_{int}^{eq})^2}\end{aligned} \tag{2.48}$$

The stability properties are inspected with the positive definite and radially unbounded LFC $V(z_1,z_2)=(1/2)\sigma^2 z_1^2+(1/2)z_2^2$ whose time derivative is given by

$$\dot{V}(z_1,z_2)=\frac{\Delta\sigma^2 z_1(z_2-\sigma z_1)-V_g\Delta z_2(z_2+\sigma y_{int}^{eq})\cos(\tilde{\chi})-V_g z_2\Delta^2\sin(\tilde{\chi})+\sigma z_2\Delta(z_2-\sigma z_1)}{\Delta^2+(z_2+\sigma y_{int}^{eq})^2} \tag{2.49}$$

$$=\Delta\frac{-\sigma^3 z_1^2-(V_g-\sigma)z_2^2-V_g z_2(\sigma y_{int}^{eq}\cos(\tilde{\chi})+\Delta\sin(\tilde{\chi}))}{\Delta^2+(z_2+\sigma y_{int}^{eq})^2} \tag{2.50}$$

inserting y_{int}^{eq} gives

$$\dot{V}(z_1,z_2)=\Delta\frac{-\sigma^3 z_1^2-(V_g-\sigma)z_2^2}{\Delta^2+(z_2+\sigma y_{int}^{eq})^2} \tag{2.51}$$

For simlicity we define $\bar{z}_1=\frac{|z_1|}{\sqrt{\Delta^2+(z_2+\sigma y_{int}^{eq})^2}}$ and $\bar{z}_2=\frac{|z_2|}{\sqrt{\Delta^2+(z_2+\sigma y_{int}^{eq})^2}}$

$\dot{V}$ is then bounded by

$$\dot{V}(z_1,z_2)\leq-(\Delta\sigma^3|\bar{z}_1|^2+\Delta(V_g-\sigma)|\bar{z}_2|^2)=-W(\bar{z}_1,\bar{z}_2) \tag{2.52}$$

$W(\bar{z}_1,\bar{z}_2)$ is positive definite under the conditions of the theorem $0<\Delta\leq\Delta_{max}$, $0<V_{g,min}\leq V_g\leq V_{g,max}$ and $0<\sigma\leq V_{g,min}$. They are reasonable as Δ and σ are design variables and V_g is a controllable state. By Theorem 4.9 in [31] the system in Equation (2.47) is UGAS.

Furthermore, notice that $W(\bar{z}_1,\bar{z}_2)\leq\bar{\lambda}_1|\bar{z}_1|^2+\bar{\lambda}_2|\bar{z}_2|^2$ for constants $\bar{\lambda}_1,\bar{\lambda}_2>0$.

In any ball $\mathcal{B}_r\{|z_2|\leq r\}, r>0$ choosing the constant $k_3>\lambda_i=\bar{\lambda}_i/(\Delta^2+(r+\sigma y_{int}^{eq})^2)$ will bound $\dot{V}$ by

$$\dot{V}(z_1,z_2)\leq-k|z|^2 \tag{2.53}$$

rendering Equation (2.47) ULES in any ball $\mathcal{B}_r$ by Thorem 4.10 in [31]. Finding the constants k_1, k_2 bounding the LFC by $k_1|z|^2 \leq V(z) \leq k_2|z|^2$ for the theorem is trivial.

The combination of UGAS and ULES gives the transformed system global κ-exponential stability [22]. It follows that the original system in Equation (2.46) is globally κ-exponentially stable as well. This concludes the proof. □

Course integral effect

An alternative to integral effect on cross-track error is integral effect on course angle error. It can be incorporated in the $f(\tilde{\chi})$ term in Equation (2.39).

Remember from Section 2.4.1 that $f(\tilde{\chi})$ needs to be an odd function. Knowing the sum of two odd functions is odd, $f(\tilde{\chi})$ can be expressed as

$$f(\tilde{\chi}) = p_{odd}(\tilde{\chi}) + \sigma \int_0^t p_{odd}(\tilde{\chi})\, dt \tag{2.54}$$

Here $p_{odd}(\tilde{\chi})$ is an odd polynomial with positive coefficients, maintaining the UGES property from Section 2.4.1. It is straightforward to verify that this is an odd function

$$f(-\tilde{\chi}) = p_{odd}(-\tilde{\chi}) + \sigma \int_0^t p_{odd}(-\tilde{\chi})\, dt = -p_{odd}(\tilde{\chi}) - \sigma \int_0^t p_{odd}(\tilde{\chi})\, dt = -f(\tilde{\chi}) \tag{2.55}$$

The integral can be realized in a digital controller with the forward Euler method because it will be a sum of odd functions maintaining the oddness. Another solution is defining an integral state, which can grow as in Section 2.4.2 or just "naively" by multiplying the course error with the integral gain.

Instead of modifying $f(\tilde{\chi})$, the integral term can be added outside the atan() function in Equation (2.39):

$$\phi_d = \text{atan}\left(\frac{V_g \cos(\gamma)\cos(\theta)}{g\cos(\chi - \psi)}\left(f(\tilde{\chi}) + \dot{\chi}_d\right) - \sin(\theta)\tan(\chi - \psi)\right) + \sigma \int_0^t p_{odd}(\tilde{\chi}) \tag{2.56}$$

Chapter 3

Method

This chapter describes the simulation setup and which guidance laws have been tested.

3.1 Simulation setup

The simulations are done with JSBSim v1.1.12 [32]. It is highly configurable and allows complex aerodynamic modeling as gust and turbulence. JSBSim permits advanced aerodynamics granting more credibility to the simulations. The Rascal 110 model is used as it is the standard model in JSBSim. The system includes airspeed sensors, GNSS, and AHRS.

The Ardupilot Plane-4.3.2 [33] was chosen for autopilot software. It is approachable but also highly configurable and open source. Ardupilot's EKF is used for state estimation, first and foremost vehicle position, velocity, and angular orientation. AOA and SSA are estimated using Equation (2.6), as done in [34]. Course angle and flight path angle are found by Equation (2.5). When the bias is added to investigate robustness, it is added directly to the guidance system to demonstrate the effect on the LOS guidance scheme. The Ardupilot TECS algorithm takes care of height and speed control. The only change is adding a LOS guidance system, substituting the L1 controller. Changes have also been made to the SITL files to control atmospheric disturbances.

Atmospheric disturbances are added with JSBSim's wind generator class, FGWinds [35]. The total amount of wind is a sum of three parts: A constant part, a cosine gust, and turbulence. The steady part is defined in the NED {n} frame and set to 15 m/s from the west for all simulations. The value of 15 m/s was chosen as it is substantial but not detrimental to the flight model with a cruise speed of about 27 m/s. It is also the value used in the simulations in Chapter 10 of [2]. For simulations including gust, the gust is divided into three periods

when it is active. The start-up period of 2.5 seconds, where the gust builds up to full magnitude from zero; the steady period of 5 seconds, where the gust stays at full magnitude; and the end period of 2.5 seconds, where it winds down to zero strength. The transient is modeled as a smooth cosine wave in the build-up and end periods. The full magnitude is 10 m/s, and it the direction is the same as the steady part in {n}. The gust starts every 15th seconds, and as the total duration is 10 seconds, there are 5 seconds of downtime in each interval. The turbulence is calculated from the Milspec model described in [36], using the Dryden spectrum from MIL-F-8785C [37]. The model takes two parameters: 'windspeed 20 feet AGL' and 'severity'. From the reference table in [35], the parameters were set to 50 ft/s and 4 to model "moderate" severity.

When comparing the performance of different guidance schemes, the wind is set to be constant to remove the element of randomness introduced with gust and turbulence. The comparisons are more fair that way. If gust and turbulence were included, the simulations would have to be redone a large number of times.

Three different paths are used in simulations. They are different variants of the same shape for simplicity. It is a circuit with a series of different angles so that the guidance laws will be tested in different conditions. The following is a short description of the paths. A more detailed description can be found in Appendix A.1. They are displayed in Chapter 4

- Path 1: a flat circuit at 100m AGL, serving as a benchmark.
- Path 2: an inclined version of Path 1, where the waypoints alternate between 100m and 400m AGL - forcing the UAV to ascend and descend such that pitch angle θ and flight path angle γ will be non-zero.
- Path 3: a "stretched out" version of Path 2, where the distances are longer, and the peaks are higher. It is used for showing the steady state behavior of the guidance laws.

Waypoints are accepted when the aircraft enters a circle of acceptance of 50 meters.

3.2 Guidance laws

This section describes the guidance laws that are tested.

3.2.1 Coordinated turn LOS

The following variants of coordinated turn LOS, derived in Section 2.4.1 are tested.

- LOS1: As presented in Gryte's thesis [2]

- LOS2: A simpler version of LOS1 where γ and θ is assumed 0
- LOS3: A more "advanced" version of LOS1 where AOA is not assumed zero
- LOS4: A more "advanced" version of LOS3 where neither AOA or SSA are assumed zero

LOS1 gives a roll command by

$$\phi_d = \text{atan}(\frac{V_g \cos(\gamma)\cos(\theta)}{g\cos(\chi-\psi)}(f(\tilde{\chi})+\dot{\chi}_d) - \sin(\theta)\tan(\chi-\psi)) \tag{3.1}$$

LOS2 gives a roll command by

$$\phi_d = \text{atan}(\frac{V_g}{g\cos(\chi-\psi)}(f(\tilde{\chi})+\dot{\chi}_d)) \tag{3.2}$$

LOS3 gives a bank command by

$$\mu_{a,d} = \text{atan}(\frac{V_g \cos(\gamma)\cos(\alpha-\theta)}{g\cos(\chi-\psi)}(f(\tilde{\chi})+\dot{\chi}_d) + \sin(\alpha-\theta)\tan(\chi-\psi)) \tag{3.3}$$

LOS4 gives a bank command by

$$\mu_{a,d} = \text{atan}(\frac{V_g \cos(\gamma)\cos(\alpha-\theta)}{g\cos(\beta-\chi+\psi)}(f(\tilde{\chi})+\dot{\chi}_d) - \sin(\alpha-\theta)\tan(\beta-\chi+\psi)) \tag{3.4}$$

LOS3 and LOS4 translate the bank command to roll by Equation (2.12).

For all the guidance laws introduced above, the desired course χ_d is given by Equation (2.21) and its time derivative by Equation (2.23).

$f(\tilde{\chi})$ is given by $f(\tilde{\chi}) = K_1\tilde{\chi}$ for simplicity.

3.2.2 Coordinated turn LOS with integral effect

The following guidance laws with integral effect are tested, introduced in Section 2.4.2. Each method will be tested with and without scaling the growth of the integral state, inspired by [8] to see its effect. The course-error integral LOS guidance laws are new contributions.

- ILOS1: LOS1 with integral effect on cross-track error developed in Section 2.4.2

- ILOS2: LOS1 with integral effect on cross-track error, but the growth of the integral state is not scaled.
- CILOS1: Course-integral LOS, where the integral term is inside the atan() term, but not scaled in any way
- CILOS2: Course-integral LOS, where the integral term is inside the atan() term, but scaled in a ILOS1 inspired way
- CILOS3: Course-integral LOS, where the integral term is outside the atan() term, but not scaled in any way
- CILOS4: Course-integral LOS, where the integral term is outside the atan() term, but scaled in a ILOS1 inspired way

ILOS1 and ILOS2 roll commands by Equation (3.1). The difference is that desired course and its time derivative are defined differently. For ILOS1 desired course is given by Equation (2.41) and its time derivative is

$$\begin{aligned} \dot{\chi}_d &= -\frac{\Delta}{\Delta^2 + (y_e + \sigma y_{int})^2}(\dot{y}_e + \sigma \dot{y}_{int}) + \dot{\chi}_p \\ \dot{y}_{int} &= \frac{\Delta y_e}{\Delta^2 + (y_e + \sigma y_{int})^2} \end{aligned} \tag{3.5}$$

ILOS2 uses the same desired course relation as ILOS1, but its time derivatives are

$$\begin{aligned} \dot{\chi}_d &= -\frac{\Delta}{\Delta^2 + (y_e + \sigma y_{int})^2}(\dot{y}_e + \sigma \dot{y}_{int}) + \dot{\chi}_p \\ \dot{y}_{int} &= y_e \end{aligned} \tag{3.6}$$

All the remaining guidance laws use the desired course χ_d from Section 3.2.1, defined in Equation (2.21).

CILOS1 and CILOS2 uses Equation (3.1) for desired roll with another course error function $f(\tilde{\chi}) = K_1\tilde{\chi} + \sigma\tilde{\chi}_{int}$

Where for CILOS1

$$\dot{\tilde{\chi}}_{int} = \sigma\tilde{\chi} \tag{3.7}$$

and for CILOS2

$$\dot{\tilde{\chi}}_{int} = \frac{\Delta\tilde{\chi}}{\Delta^2 + (\tilde{\chi} + \sigma\tilde{\chi}_{int})^2} \tag{3.8}$$

For CILOS3 and CILOS4 $f(\tilde{\chi}) = K_1\tilde{\chi}$ as Section 3.2.1, but the roll command is different. The integral state is added outside of the atan-function.

$$\phi_d = \text{atan}(\frac{V_g \cos(\gamma)\cos(\theta)}{g\cos(\chi-\psi)}(f(\tilde{\chi}) + \dot{\chi}_d) - \sin(\theta)\tan(\chi-\psi)) + \tilde{\chi}_{int} \tag{3.9}$$

where for CILOS3 the integral state is given by Equation (3.7) and for CILOS4 it is stated in Equation (3.8)

3.2.3 L1

The Ardupilot implementation of the L1 controller introduced in Section 2.2.2 will be a reference point for the LOS guidance systems. It is implemented with integral effect, the details described in Section 2.3.2. To test L1 without integral effect, the integral gain, which will also be denoted σ, is set to zero for simplicity.

3.3 Tests

The following tests were carried out:

T1 **Atmospheric disturbances**. The tuning of LOS1 was validated by having the aircraft follow Path 2 with atmospheric disturbances: gusts and turbulence along with the steady wind.

T2 **Including AOA and SSA in coordinated-turn-inspired LOS**. The validity of Assumption 6 and the effect of including more "aerodynamics" was inspected by comparing the performance of LOS1, LOS2, LOS3, and LOS4. Path 1 and Path 2 were tested to see if there was a difference between level and ascending/descending flight. The wind is kept steady to reduce randomness.

T3 **Robustness**. The robustness of coordinated-turn-inspired LOS was investigated by adding bias to AOA, SSA, heading, and pitch angle to understand better the risks of including potentially biased estimates in the guidance system. Bias in roll angle is not tested because it is not used in the guidance system, but the attitude controller, whose robustness is not a focus of this thesis. A level path was used when testing heading bias for simplicity. For AoA/SSA and pitch angle bias, Path 2 was used as the estimates would have a larger numerical value, and any bias would therefore influence the guidance system more.

T4 **Integral effect**. The controllers in Section 3.2.2 were tested against each other to investigate how they performed and find any noticeable differences in their performance. The integral gain was also tested for two values: $\sigma = 0.1$ and $\sigma = 1$. Any value a magnitude less than 0.1 seemed in initial testing to not have any evident influence, and any value a magnitude larger would generate large oscillations and approach the upper bound found in Section 2.4.2.

T5 **Comparison to L1 controller**. LOS1 and ILOS1 were tested against L1 with and without integral effect to compare what has been explored in this thesis against the Ardupilot standard to give an idea of how LOS performs against the obvious alternative.

The tests T2-T5 are done without turbulence and gusts to reduce randomness and make the comparisons more reasonable. The LOS parameters are found from the tuning guidelines developed from the linear analysis in Chapter 10 of [2]: $\Delta = \frac{V_g K_1}{\omega_0^2}, K_1 = \omega_0(\zeta \pm \sqrt{\zeta^2 - 1})$. Control damping and period are parameters in Ardupilot. For all tests NAVL1_PERIOD = NAVLOS_PERIOD = 17s and NAVL1_DAMPING = NAVLOS_DAMPING = 1. The LOS and L1 period/damping are equal to allow a fair comparison between the two guidance schemes. The damping was set to 1 to ease the expression for K_1 above, and the period is the default value in Ardupilot [33]. The $\dot{\chi}_p$ is set to zero as the path consists of straight line segments and is only non-zero the instant the subsequent waypoint changes.

The attitude and TECS controllers are left with default values.

Chapter 4

Results

This chapter displays the results from the simulations. The sections are ordered in the same way as the list of tests in Section 3.3.

4.1 Atmospheric disturbances

To validate the tuning, the aircraft follows Path 2 using LOS1 while experiencing gusts and turbulence in combination with steady wind. The result is displayed in Figure 4.1 showing path following with relevant angles and Figure 4.2 depicting cross-track error, altitude, and airspeed. The effect of the gust and turbulence might be best seen in the latter, with the periodic oscillation in airspeed and the altitude drops. The regular dips in altitude in Figure 4.2 could be signs of stall from turbulence and gust.

The atmospheric effects make it difficult for the guidance system to drive the cross-track error to zero, but the cross-track error has nice convergence in the transient. Therefore it can be argued that the tuning of the guidance system is satisfactory. Furthermore, the LOS guidance law is shown to track the desired path, supporting the results of simulations and experiments in [2].

The performance of the roll and pitch angle controllers are seen in Figure 4.3 with steady wind, turbulence, and gust and in Figure 4.4 with only steady wind. They are shown to track the desired angles well, except for some overshoot in the roll controller when the step in reference is large. When the roll angle is large, the pitch angle controller can struggle with following the desired reference. This makes sense as the lift force will be reduced for large roll angles, making it difficult to control pitch with the elevator.

The lower-level controllers will behave similarly as only the guidance system is experimented with in the following sections. Therefore the most complete system

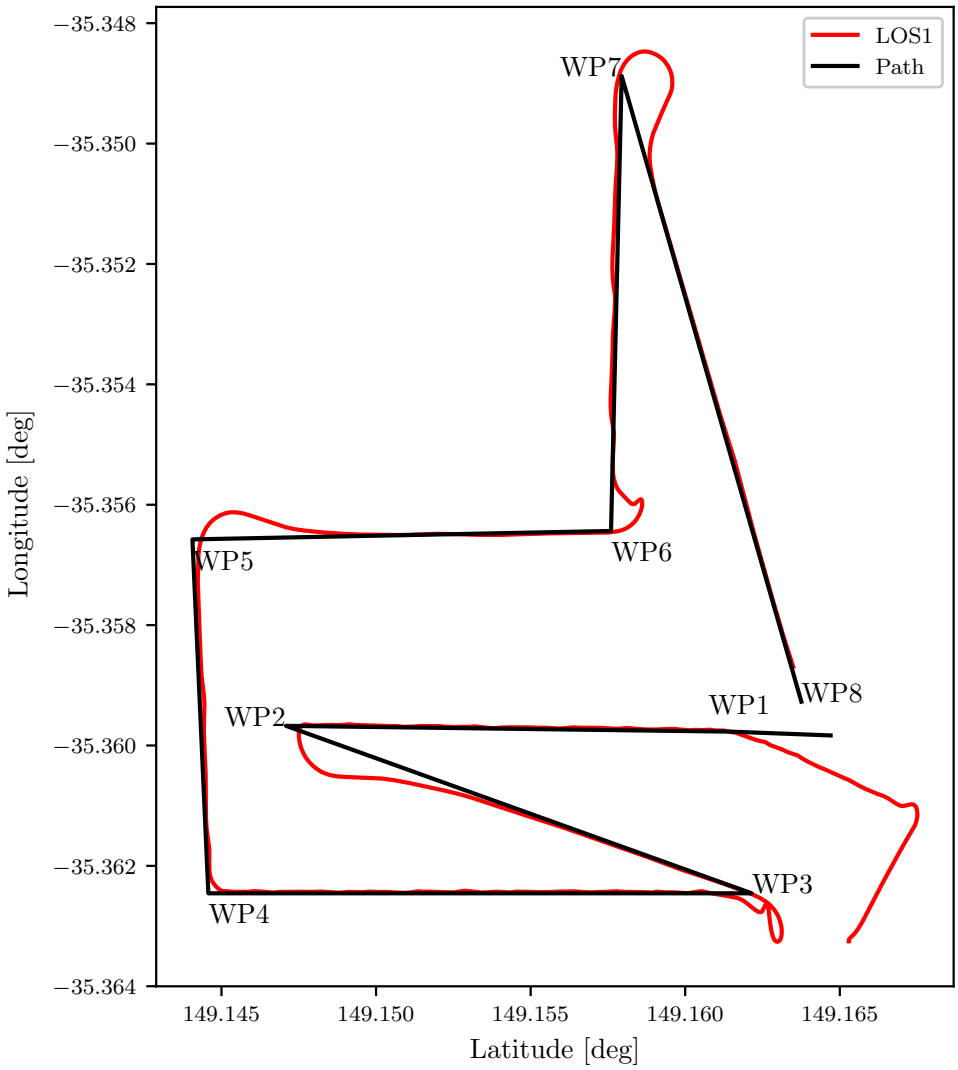

(a) Path following

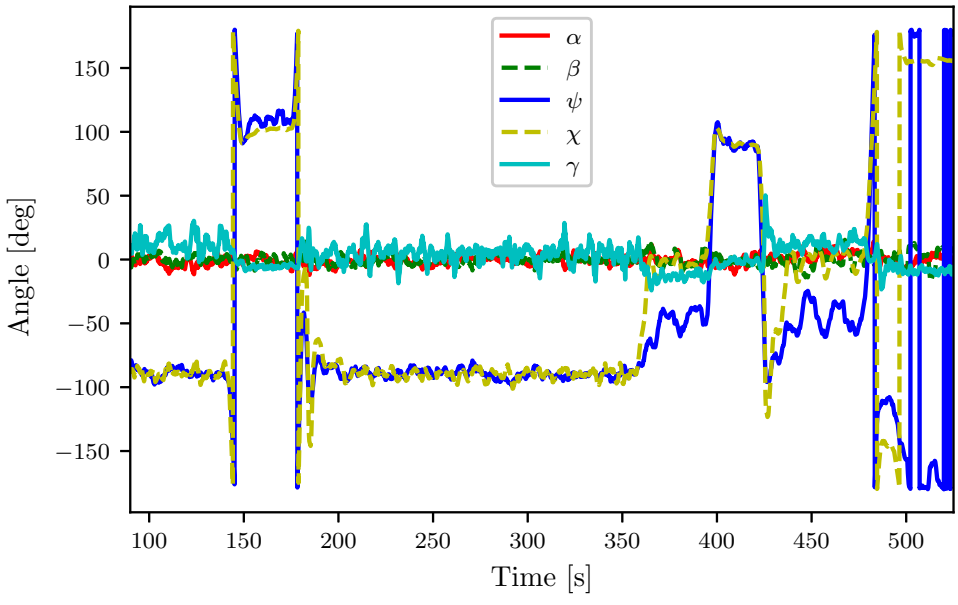

(b) angles between WP2 and WP8

Figure 4.1: Path following and angles from LOS1 simulations using Path 1 and being subjected to atmospheric disturbances: steady wind, turbulence, and gust.

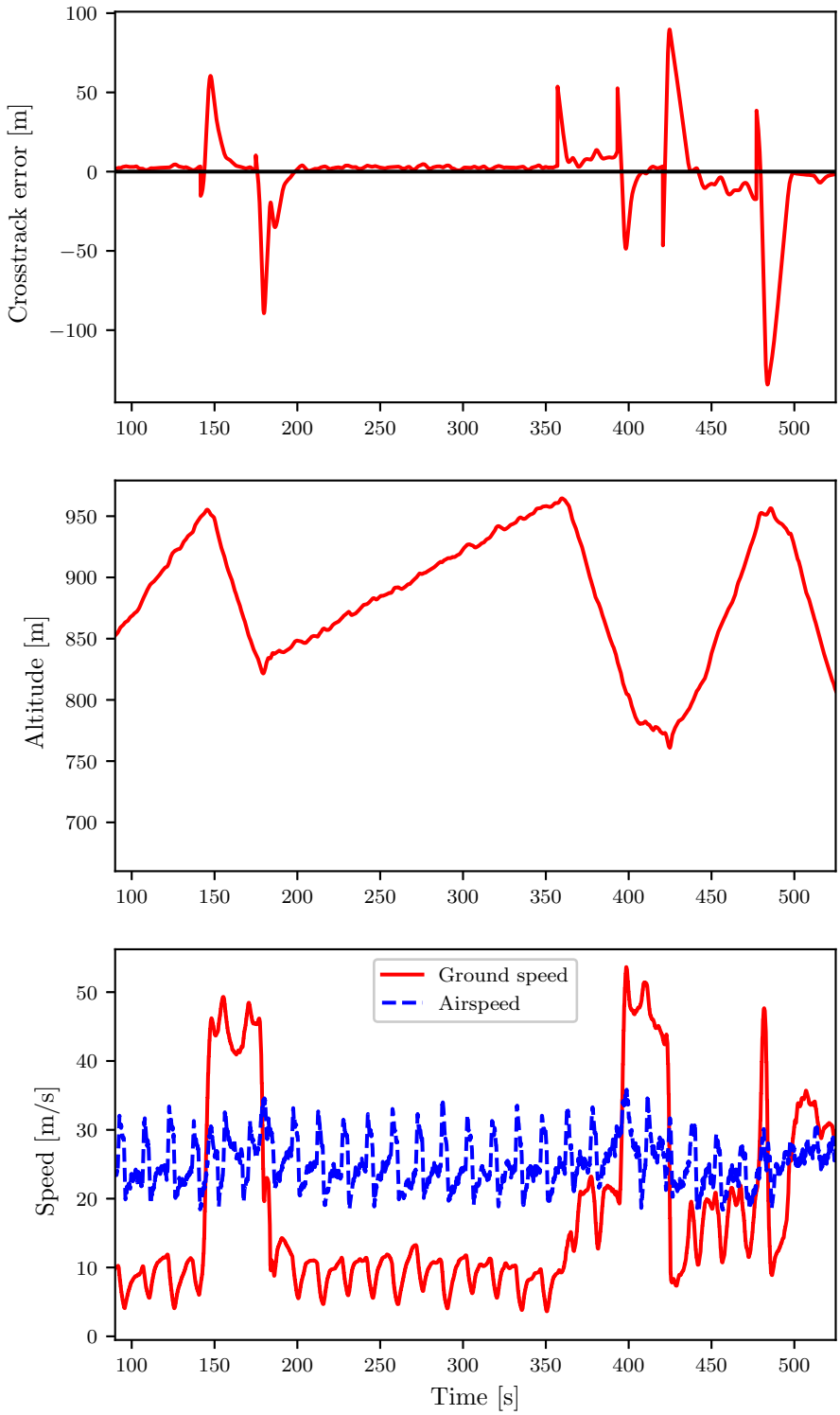

Figure 4.2: Crosstrack error, altitude, ground and airspeed from LOS1 simulations using Path 2 and being subjected to atmospheric disturbances: steady wind, turbulence, and gust.

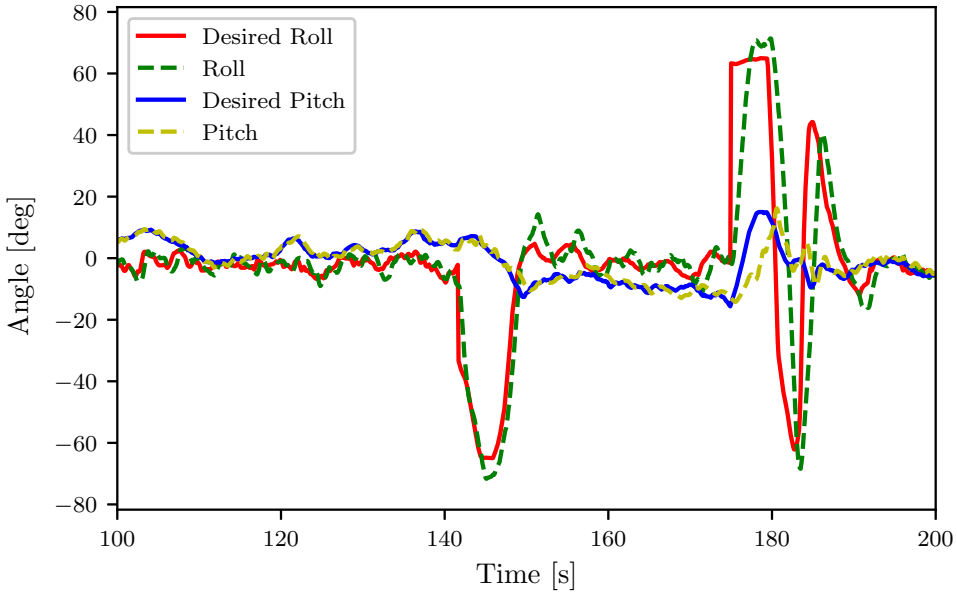

(a) Between WP2 and WP3

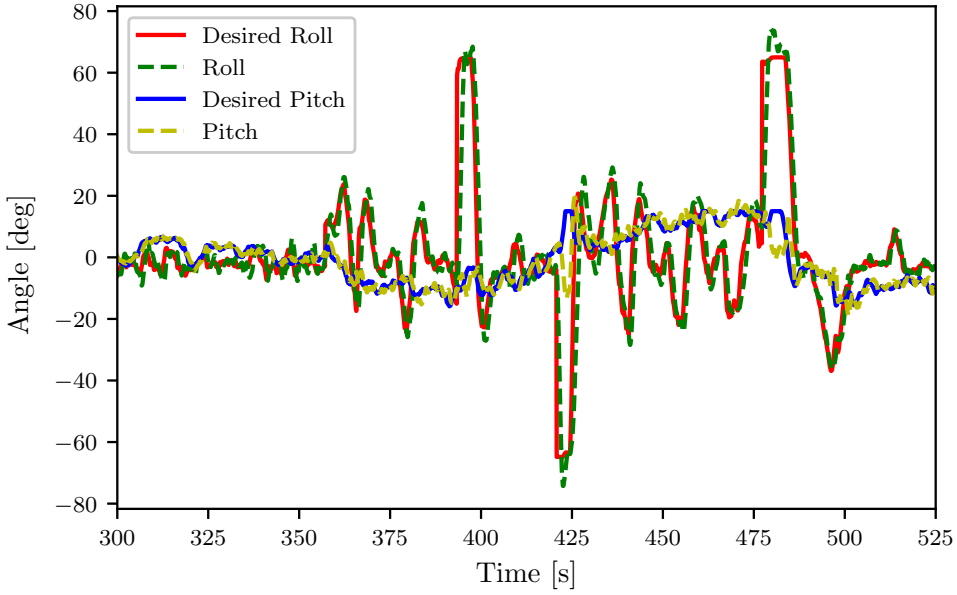

(b) Between WP4 and WP8

Figure 4.3: Desired and simulated roll and pitch angles from LOS1 simulations using Path 2 and being subjected to steady wind, turbulence, and gust

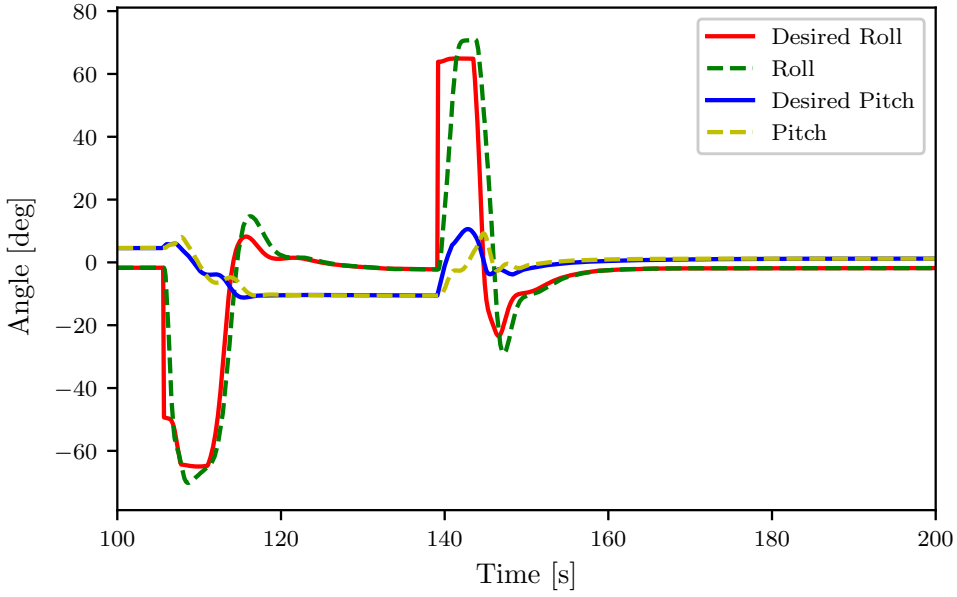

(a) Between WP2 and WP3

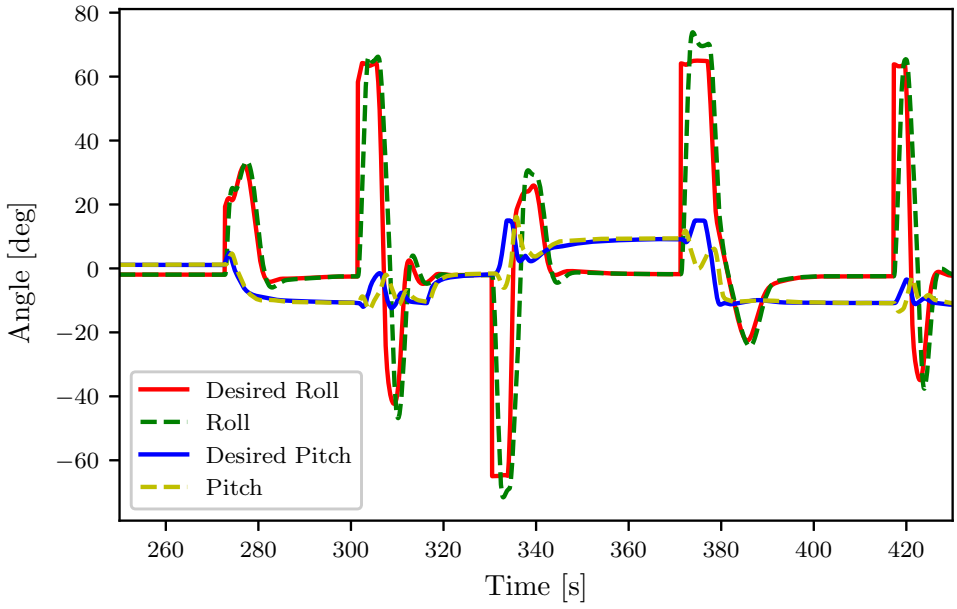

(b) Between WP4 and WP8

Figure 4.4: Desired and simulated roll and pitch angles from LOS1 simulations using Path 2 and being subjected to steady wind only

information is shown in this section, while only information relevant to guidance is shown later on.

4.2 Including AOA and SSA in coordinated-turn-inspired LOS

Figure 4.5 and Figure 4.6 display path following and simulated states following Path 1 with steady wind. The same information is plotted from simulations with Path 2 and steady wind in Figure 4.7 and Figure 4.8.

The guidance laws perform very similarly for level flight. This could be because the angles separating them are mostly small in Figure 4.5b. The numerically insignificant angle of attack and sideslip angle estimates in Figure 4.5b support the validity of A6. This is further backed by Figure 4.7b, AOA and SSA are small, and the performance is largely the same with varying flight path angle in Figure 4.7a and Figure 4.8. When it comes to the accuracy of the AOA and SSA estimates, the usual cause of error is the stochastic characteristic of wind and other atmospheric effects. This is not the case here, as the wind was steady for these simulations with no gusts or turbulence. The other input to AOA and SSA estimation is the velocity estimates in {n}, which are corrected by accurate GNSS measurements.

Including pitch and FPA does not seem to have much effect either. LOS2 performs similarly to the other LOS variants in Figure 4.6 and Figure 4.8. When these angles are small, the difference in performance is negligible. An interesting exception is when the UAV is hit by crosswind while ascending or descending, which can be seen in the steady-state cross-track error offset LOS1, LOS3, and LOS4 have in the line segments WP4-WP5 and WP6-WP8 in Figure 4.8, but not in Figure 4.6. LOS2 does not have this offset.

A possible explanation is that Assumption A5 is not valid when the airspeed is not horizontal, making the approximation of air-relative course angle $\chi_a = \psi + \beta$ inaccurate. This makes sense intuitively; the airspeed will have a non-zero vertical component while ascending or descending with horizontal wind. Furthermore, it can be seen in Figure 4.7b that the difference between course and heading $\chi - \psi$ is largest under crosswind - which checks out as the UAV has to face partly in the direction of the wind to maintain its course. This means that the $\sin(\theta)\tan(\chi - \psi)$ term for LOS1 in Equation (3.1), which contains the approximation of χ_a, will give a noteworthy contribution assuming the pitch angle θ is not negligible. LOS2 does not have this term in Equation (3.2) and is therefore not affected. However, it also uses the approximation in Assumption A5 in the cosine factor in the denominator, but so do all the other LOS variants, and it will not make a difference in the comparison.

The inclusion of flight path angle and pitch estimates in LOS1 could also be sus-

pected of causing the offset, but they don't impact the performance the same way in the line segments WP1-WP4 and WP5-WP6. They are also substantially lower than the difference of course and heading in Figure 4.7b. If one doubted the validity of Assumption A4, Figure 4.8 would demonstrate that the roll angle is near zero during the steady state offset. This supports the wings-level flight requirement for Assumption A4 and does not give any reason to doubt the approximation of the air-relative path angle $\gamma_a = \theta - \alpha$. LOS3 and LOS4 do also have the offset, showing that lack of α or β is not the reason.

4.3 Robustness

Figure 4.9 shows how bias in AOA/SSA estimate affects performance by increasing steady-state error. Note that a larger bias gives a worse performance, as expected.

Figure 4.10 and Figure 4.11 display the effect of pitch bias in LOS1 from simulations with Path 2 and steady wind. Note that a larger bias gives a more steady-state cross-track offset. Figure 4.12 and Figure 4.13 show the effect of heading bias applied to LOS1 following Path 1 with steady wind. Note that a larger bias gives more cross-track error oscillations.

A possible explanation for pitch bias causing offset and heading bias causing overshoot can be found in the properties of the atan-function encapsulating the expression for the desired roll in Equation (3.1). Adding bias to the pitch estimate in the $\cos(\theta)$-factor in the nominator will decrease the argument of the atan function, which gives out less desired roll - visible in Figure 4.11. On the other hand, the heading estimate in the $\cos(\chi - \psi)$-factor is in the denominator for the argument of the atan-function. A bias in the cosine function will therefore decrease the value of the denominator, causing the argument of the atan function and, consequently, the outputted desired roll to be larger as displayed in Figure 4.13. This could cause increasing oscillations of the cross-track error when the heading estimate increases.

4.4 Integral effect

Figure 4.14 displays the error angles of LOS1 in both level and climbing flight. It can be seen that the course error signal has both a higher overshoot and steady-state error than the roll error. This means that integral action on error angles would be better directed at reducing the course error over roll error. It should also be noted that in the transient Assumptions A7-A8 are not valid. However, they seem reasonable when approaching a steady state. The cross-track error is approximately constant and small. It can also be seen that the pitch error is insignificant.

Figure 4.15 and Figure 4.16 show all the different integral effect guidance laws

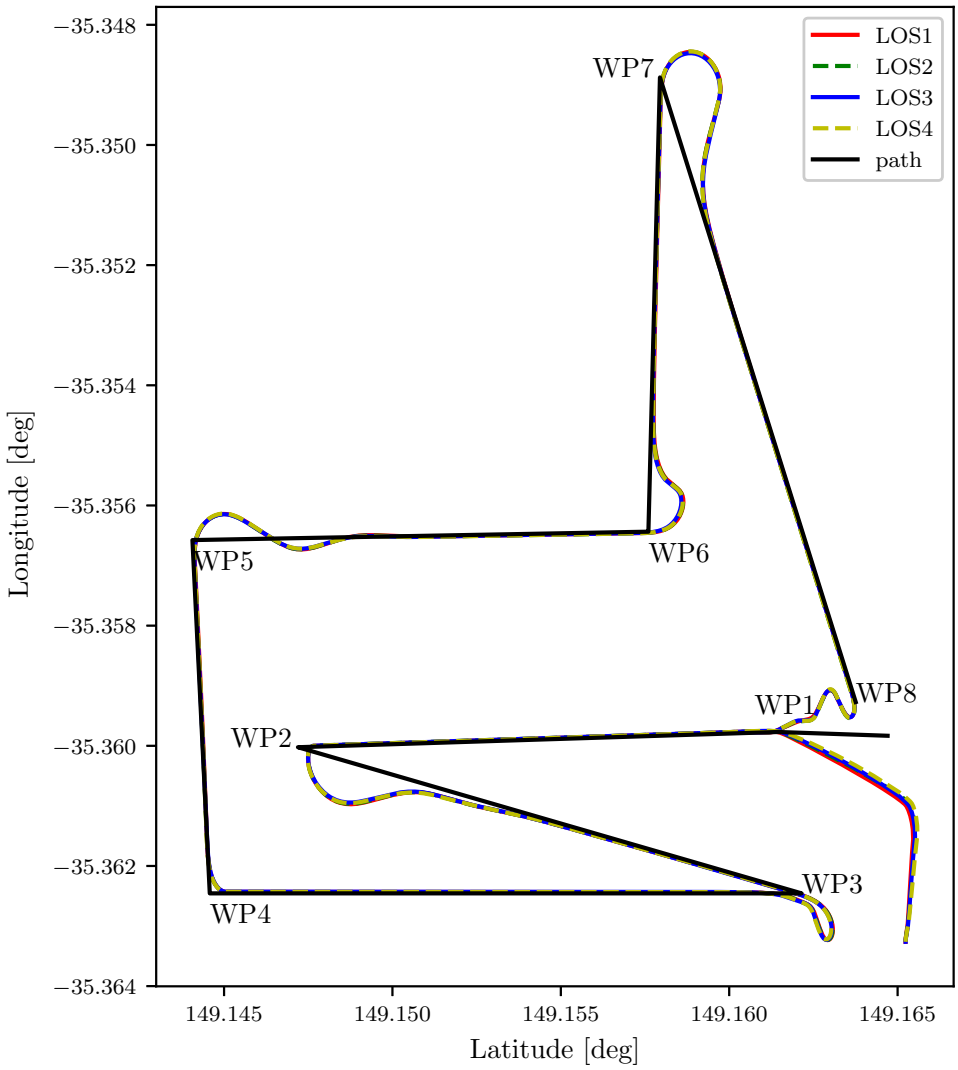

(a) Path following

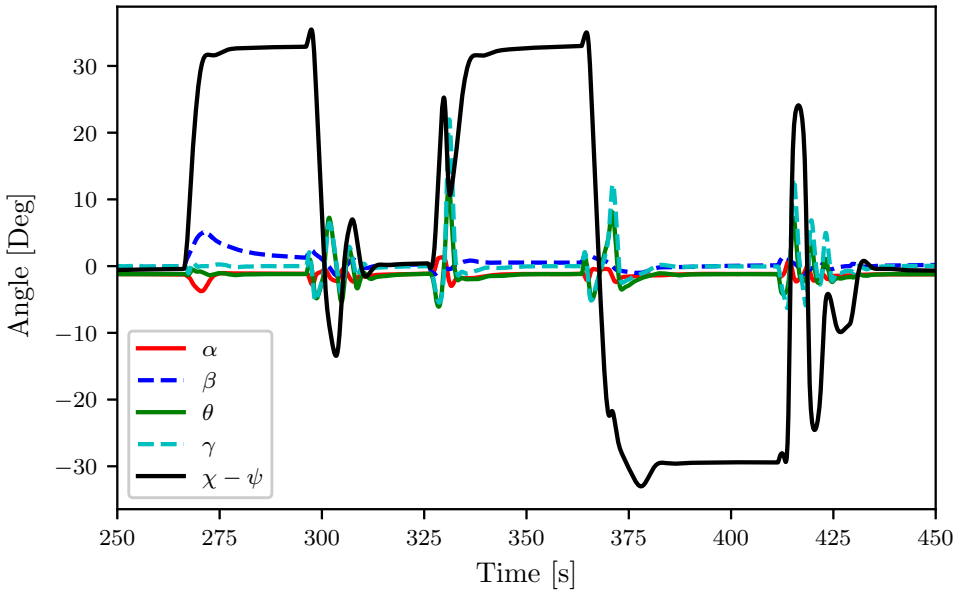

(b) angles between WP4 and WP8

Figure 4.5: Path 1 following and angles from simulations with constant 15 m/s from the west.

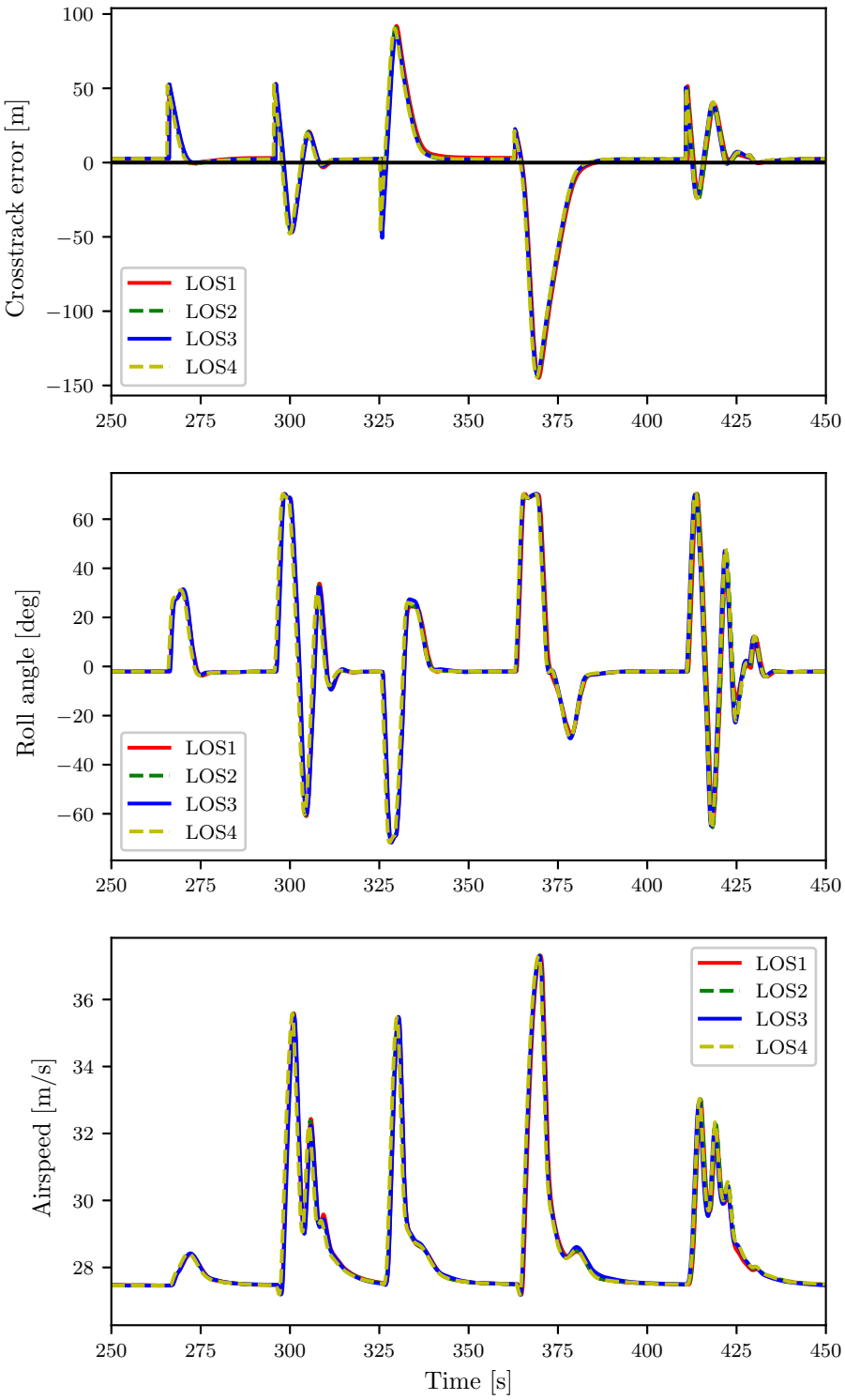

Figure 4.6: Crosstrack error, roll angle, and airspeed from simulations following Path 1 between WP4 and WP8 with constant 15 m/s wind from the west.

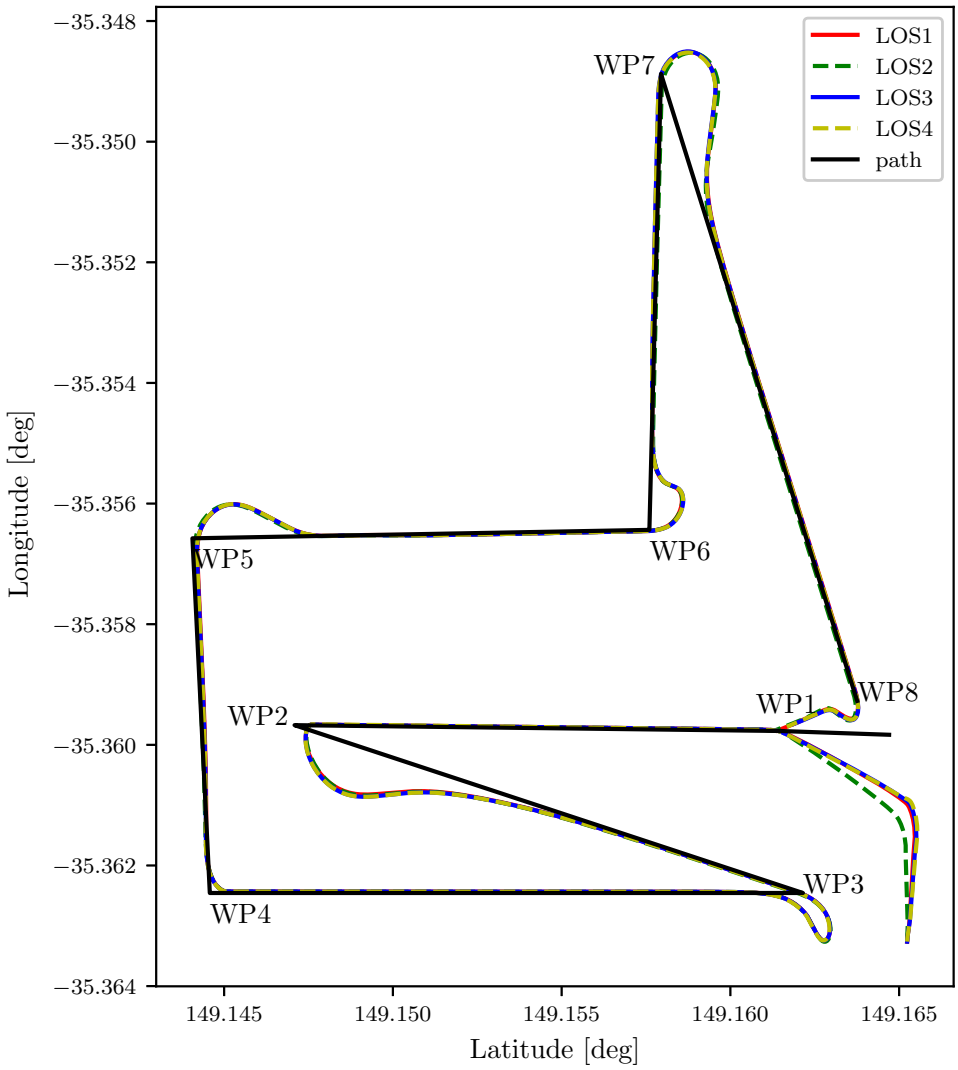

(a) Path following

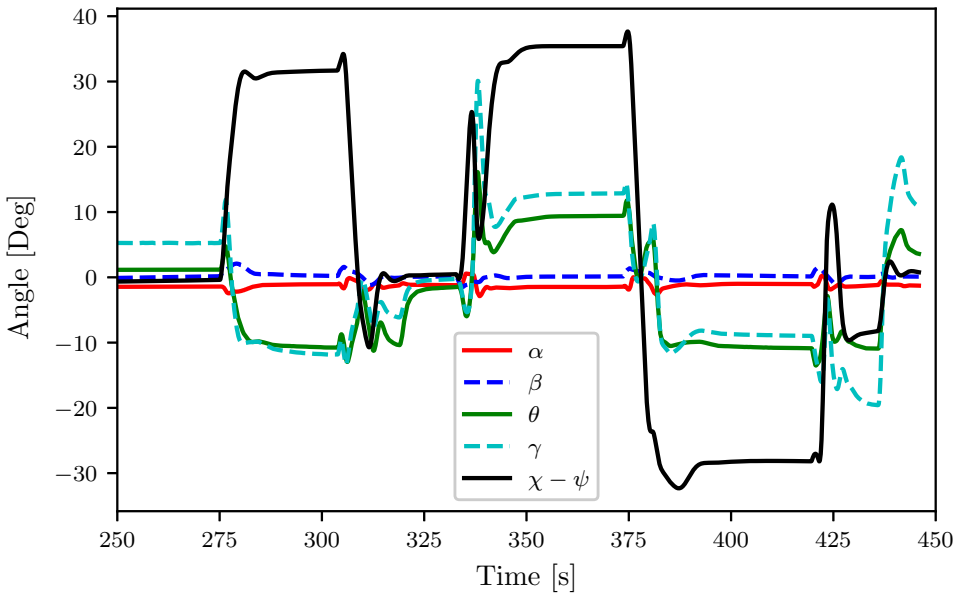

(b) angles between WP4 and WP8

Figure 4.7: Path following and angles from simulations using Path 2 and constant 15 m/s from the west.

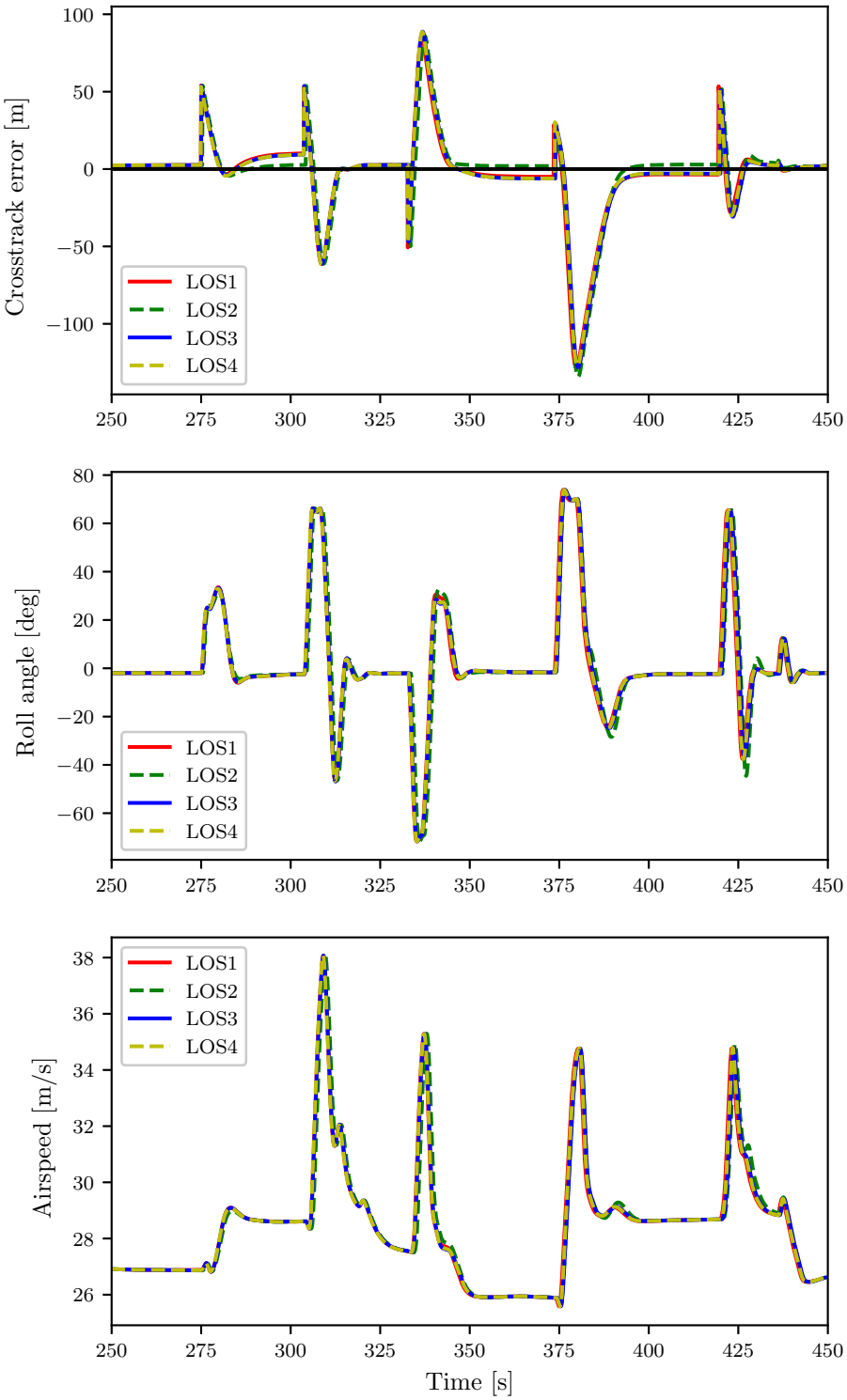

Figure 4.8: Crosstrack error, roll angle, and airspeed simulations using Path 2 WP4 and WP8 and constant 15 m/s from the west.

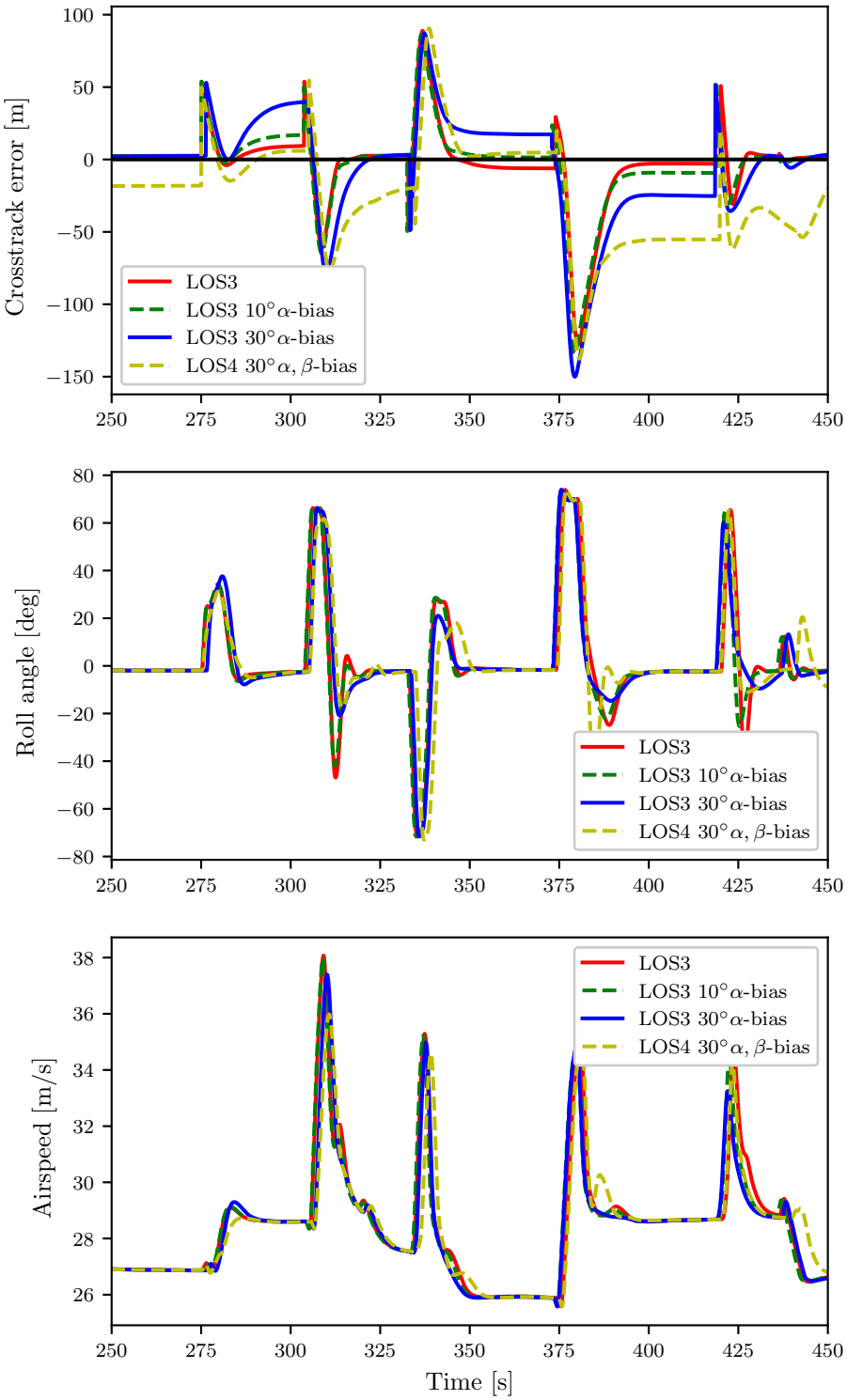

Figure 4.9: Crosstrack error, roll angle, and airspeed simulations between WP4 and WP8 using Path 2 and constant 15 m/s from the west. Bias added to AOA and/or SSA estimate

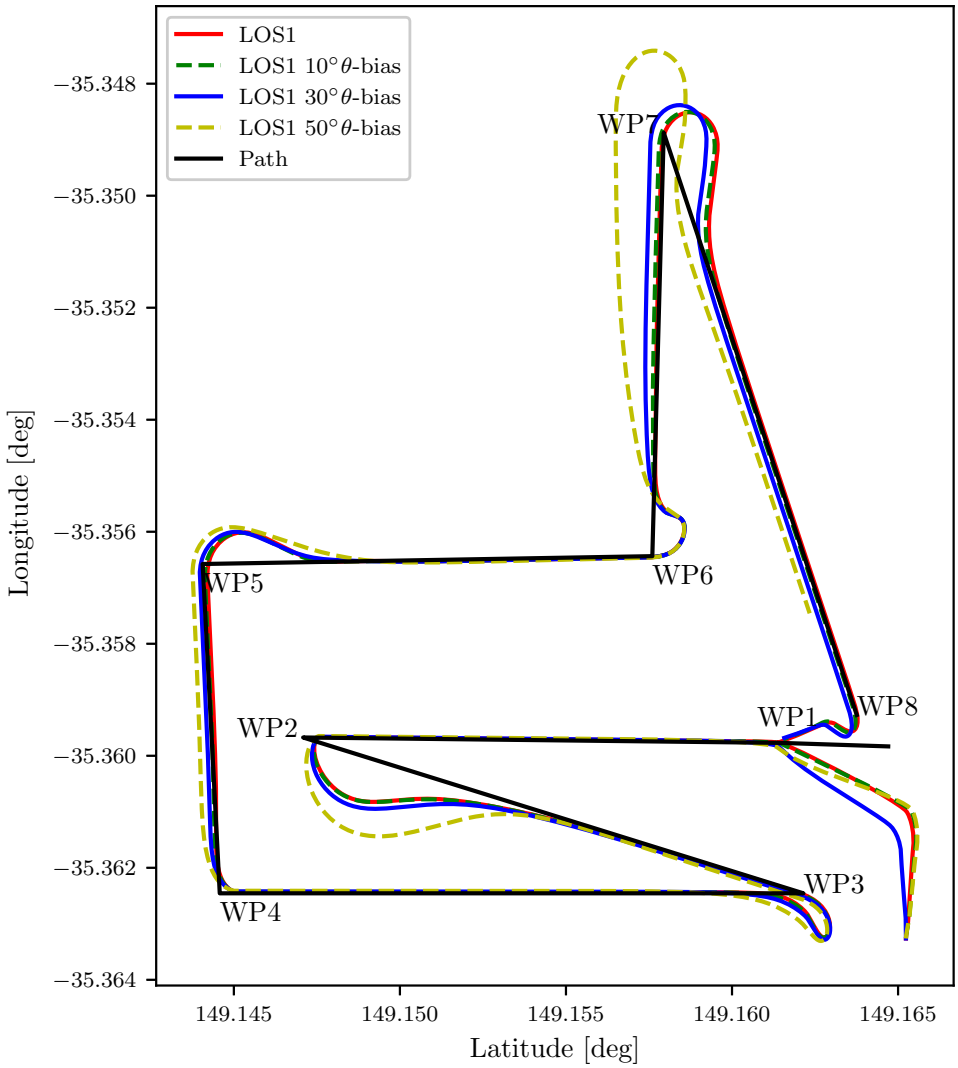

Figure 4.10: Path following from simulations using Path 2 and receiving constant 15 m/s from the west with varying pitch bias

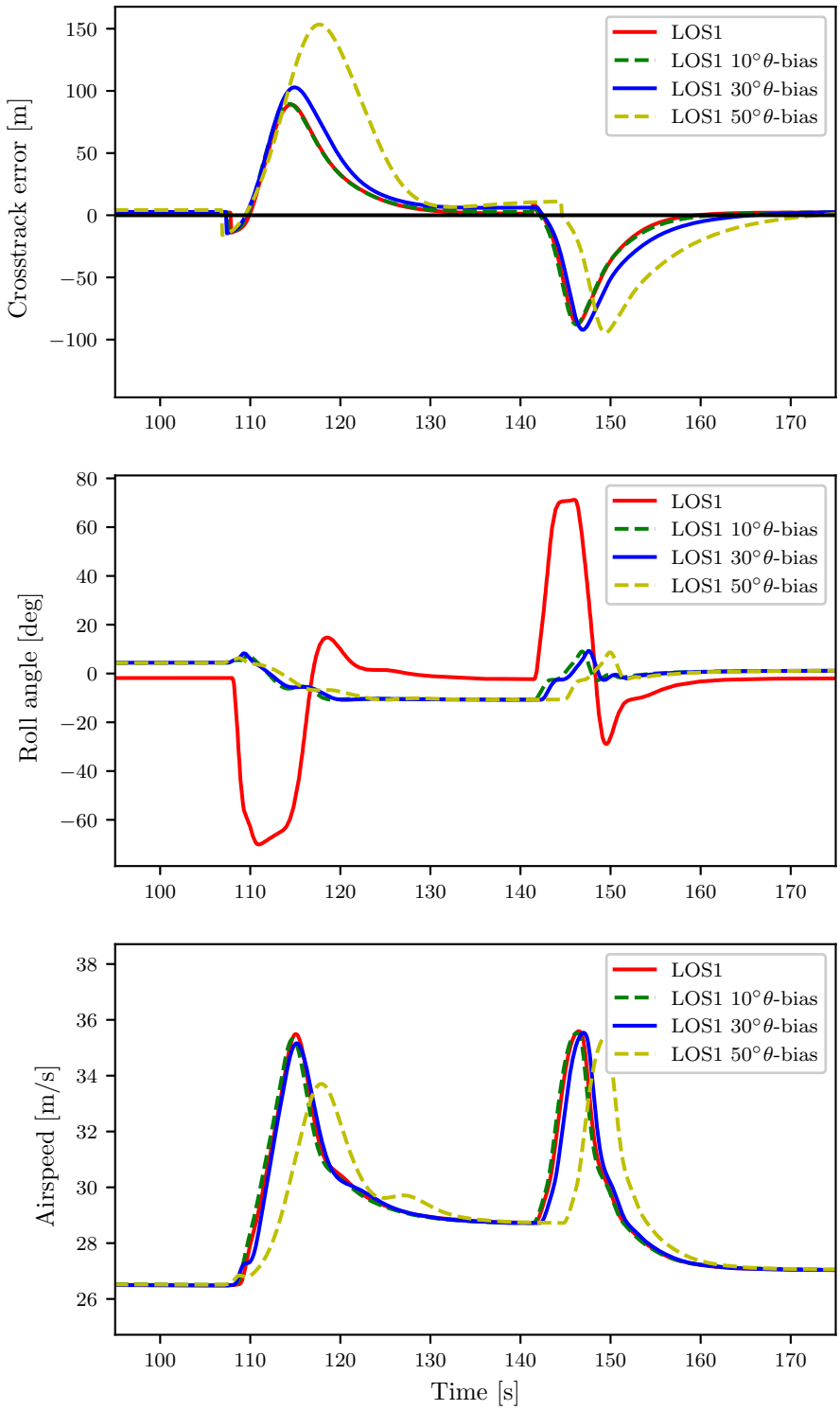

Figure 4.11: Crosstrack error, roll angle, and airspeed simulations between WP1 and WP2 using Path 2 and constant 15 m/s from the west with varying pitch bias

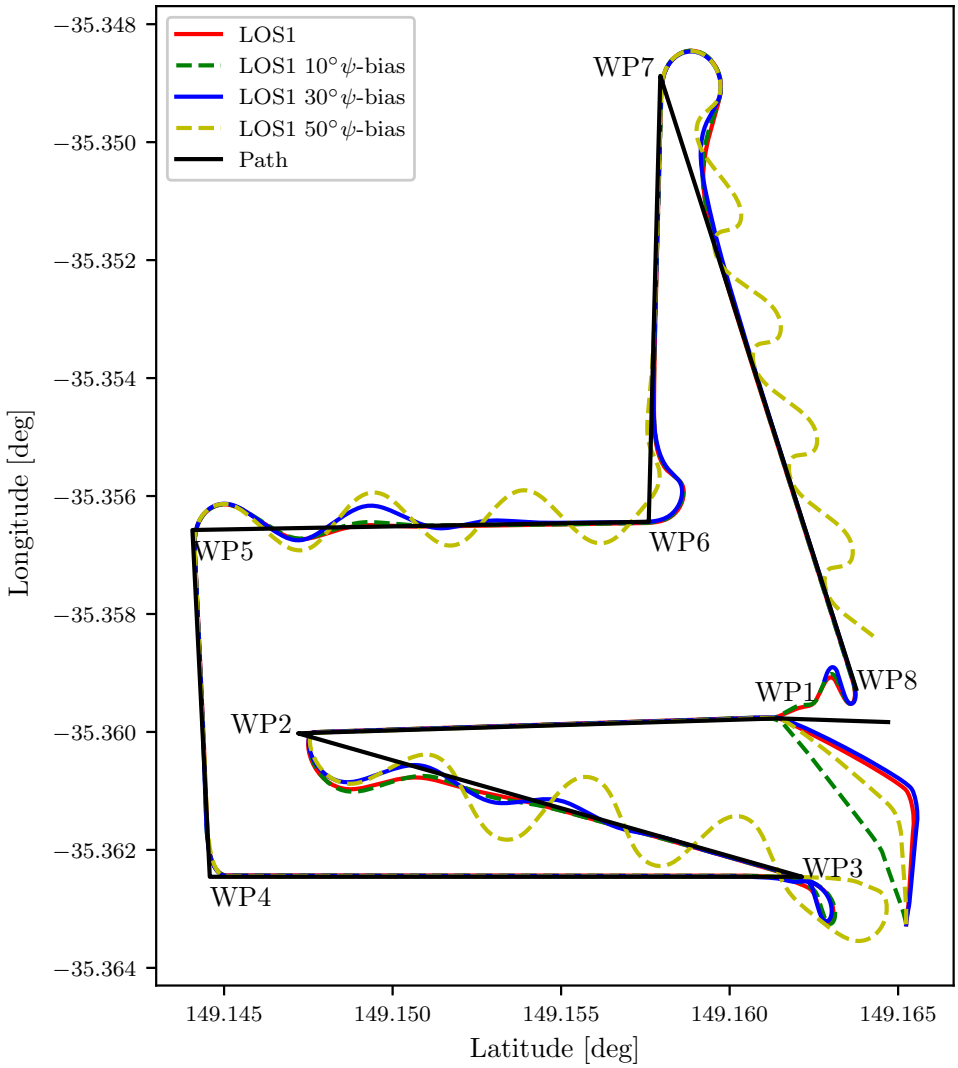

Figure 4.12: Path following from simulations using Path 1 and constant 15 m/s from the west with heading bias

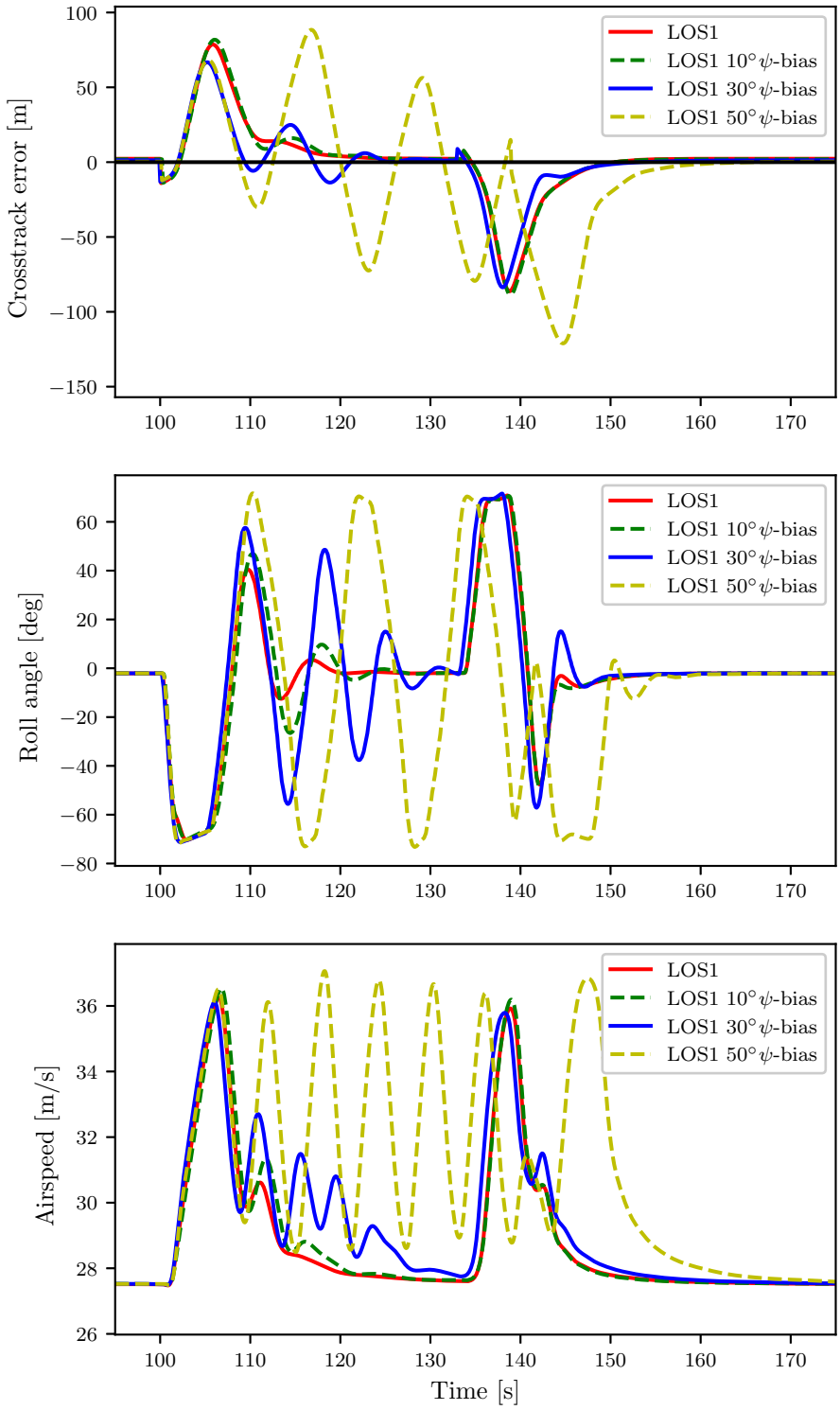

Figure 4.13: Crosstrack error, roll angle, and airspeed simulations between WP1 and WP2 using Path 1 and experiencing constant 15 m/s from the west with heading bias

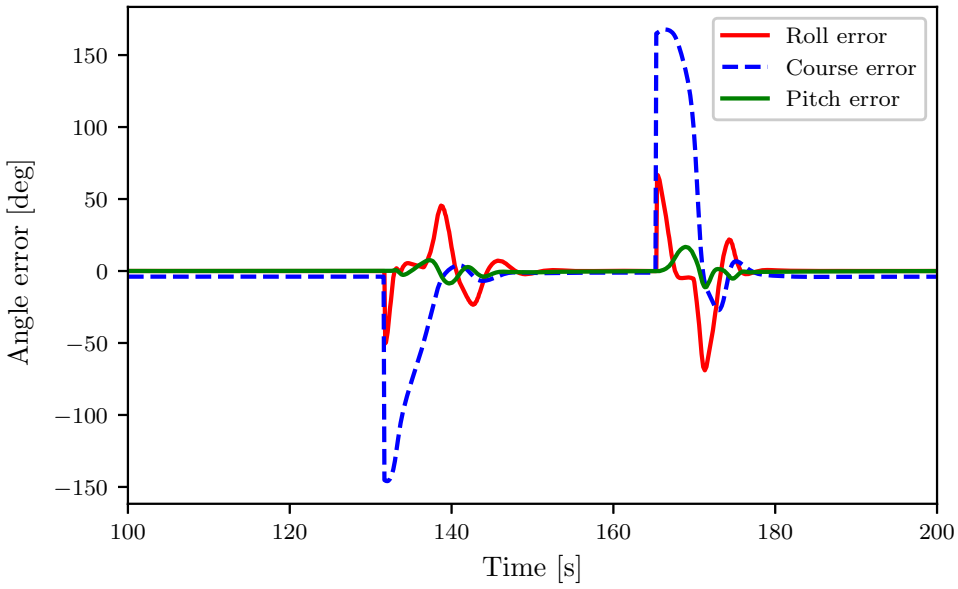

(a) Level flight between WP1 and WP3, following Path 1

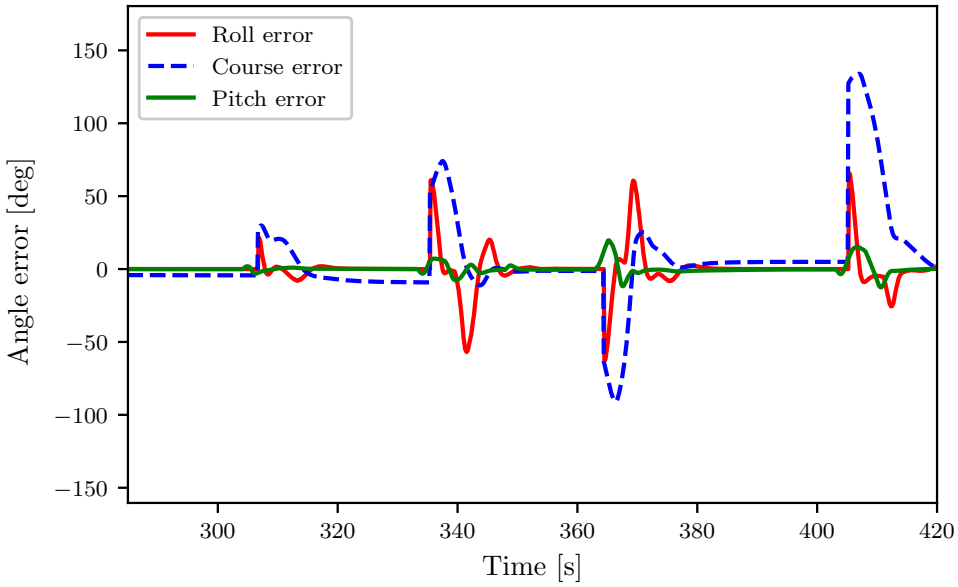

(b) Ascending and descending flight between WP5 and WP8, following Path 2

Figure 4.14: Error angles for LOS1

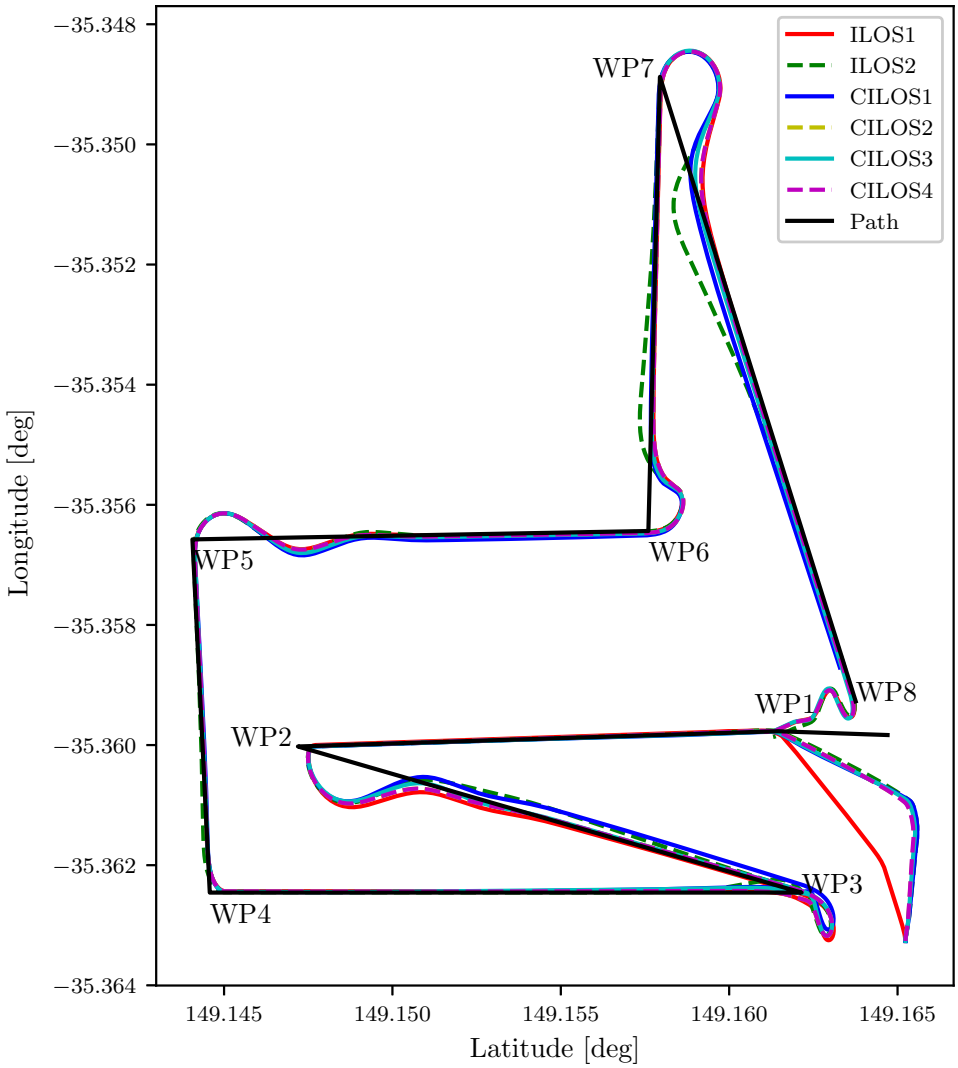

Figure 4.15: Path following from simulations using Path 1 and constant 15 m/s from the west. Integral gain $\sigma = 0.1$

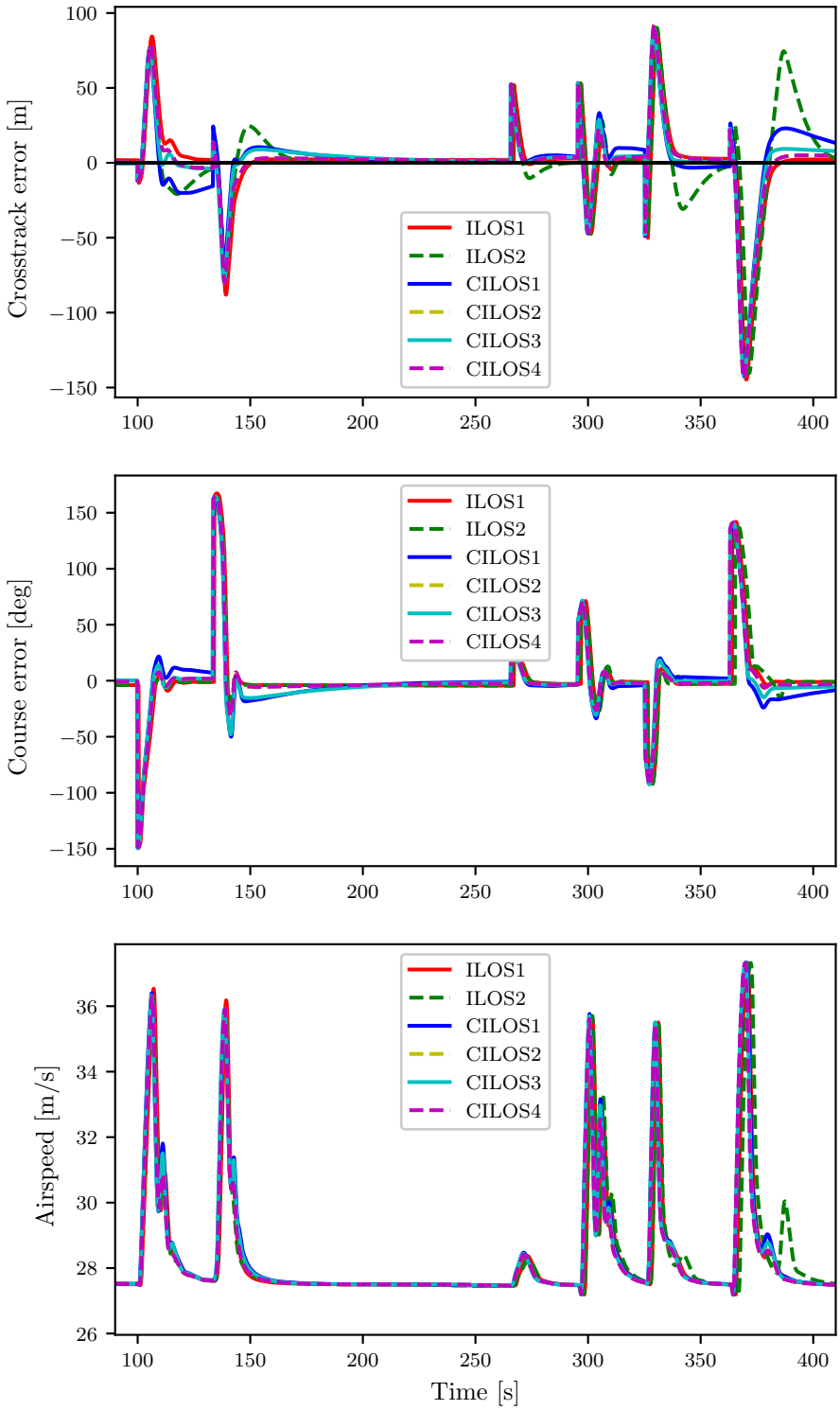

Figure 4.16: Crosstrack error, roll angle, and airspeed simulations using Path 1 and constant 15 m/s from the west. Integral gain $\sigma = 0.1$

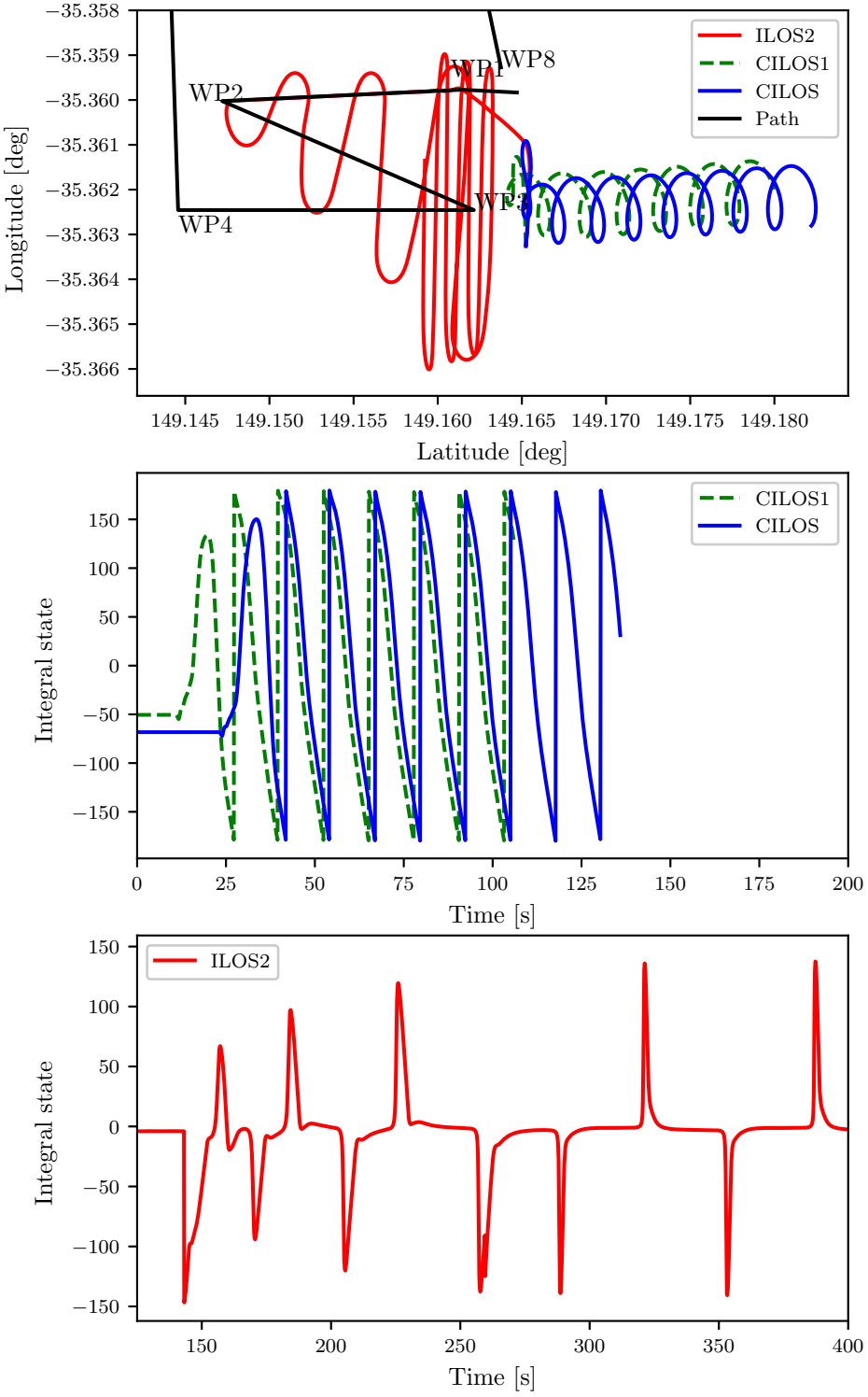

Figure 4.17: Path following and integral state from simulations using Path 1 and constant 15 m/s from the west. Integral gain $\sigma = 1$

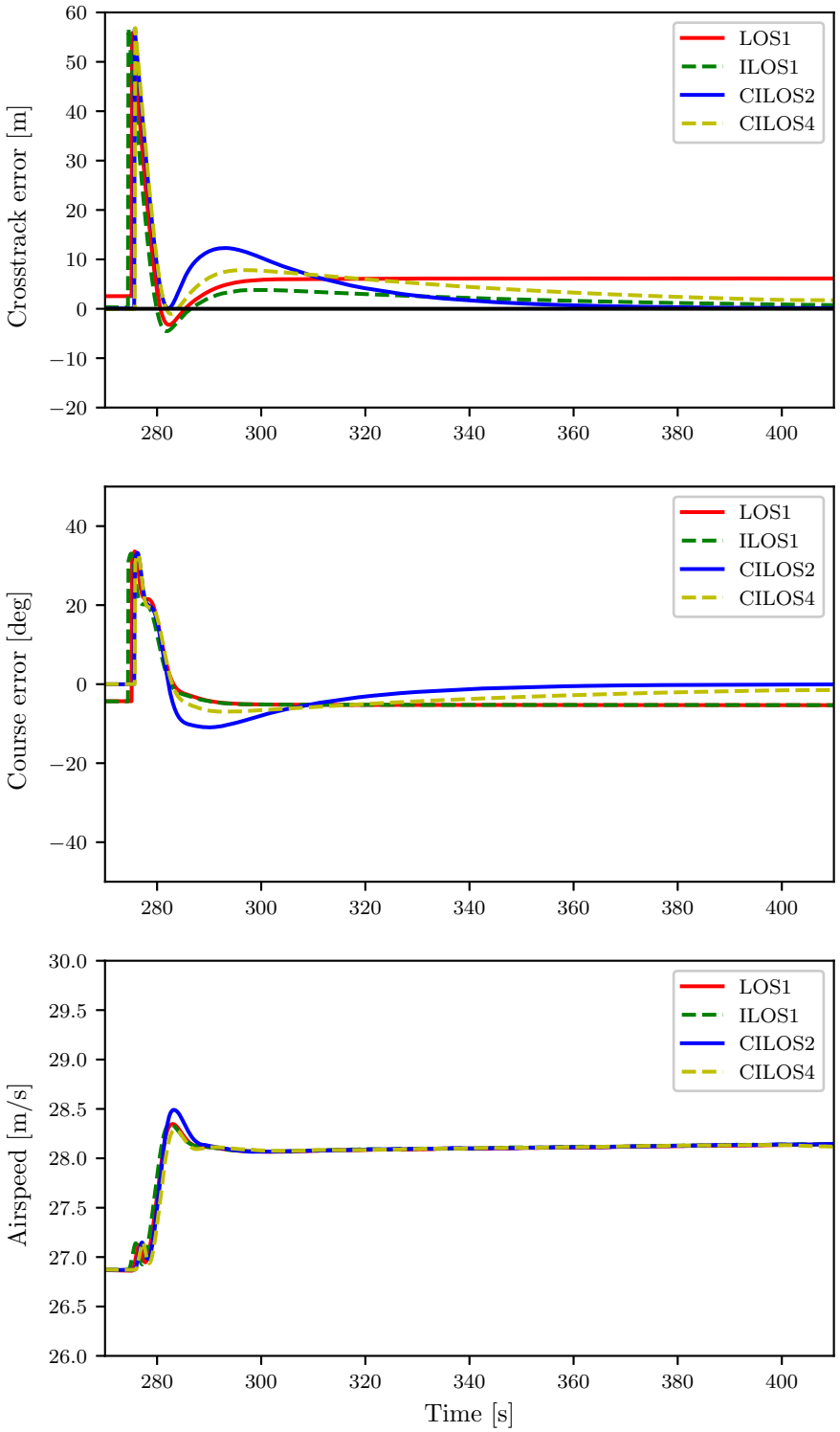

Figure 4.18: Crosstrack error from simulations between WP4 and WP5 using Path 3 experiencing constant 15 m/s from the west with integral gain $\sigma = 1$.

completing the course with integral gain $\sigma = 0.1$, being viable options. It can be seen that ILOS, CILOS1, and CILOS3, which do not scale the integral state in any way, have larger overshoot than their counterparts. This is expected as the point of scaling the integral state in a [8]-inspired way is intended to reduce overshoot. Figure 4.17 shows that these non-scaled integral state growth schemes can become unstable for larger integral gain ($\sigma = 1$) as the integral state grows large. However, choosing a too-high integral gain would also be detrimental to ILOS1, as the stability proof in Section 2.4.2 sets a bound on σ. On the other hand, the bound on the integral gain is higher for the [8]-inspired scaled integral gain schemes. This can be seen in Figure 4.18, which shows that they remove the steady-state error in simulations following Path 3 with $\sigma = 1$. Here the larger integral gain gives more integral action. The course integral schemes have more overshoot but drive as expected course error to zero. ILOS1 drives the cross-track error to zero even though the course error is not zero. This is not important as the cross-track error is the main parameter for evaluating the effectiveness of a guidance system.

4.5 Comparison to L1 controller

Figure 4.19 shows path following of ILOS1/LOS1 and L1 with and without integral effect. In Figure 4.20, the L1 controllers have higher overshoot than the LOS controllers in the turn after WP1, while the guidance laws with integral effect also have higher overshoot than their counterparts without it. In Figure 4.21, it can be seen that the performance of the L1 and LOS guidance laws are more similar, in addition to integral effect removing steady-state error for both LOS and L1. ILOS has $\sigma = 1$.

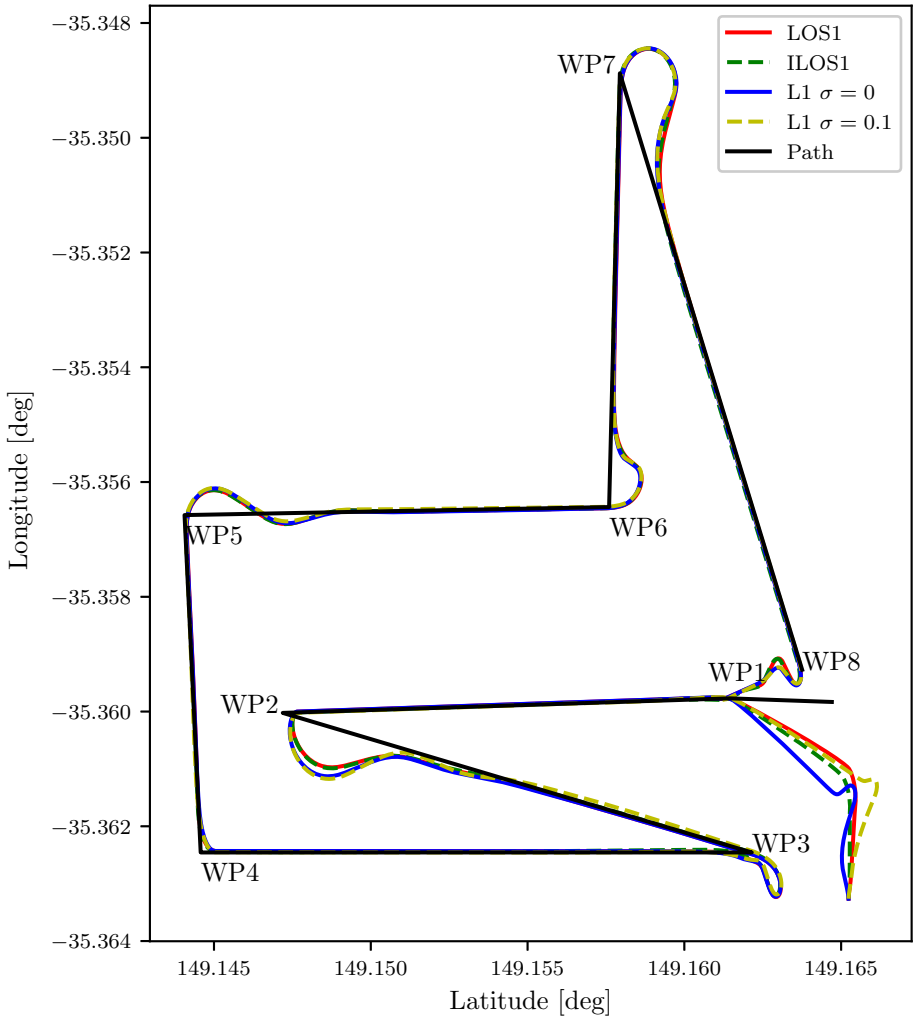

Figure 4.19: Path following path 1 with steady wind

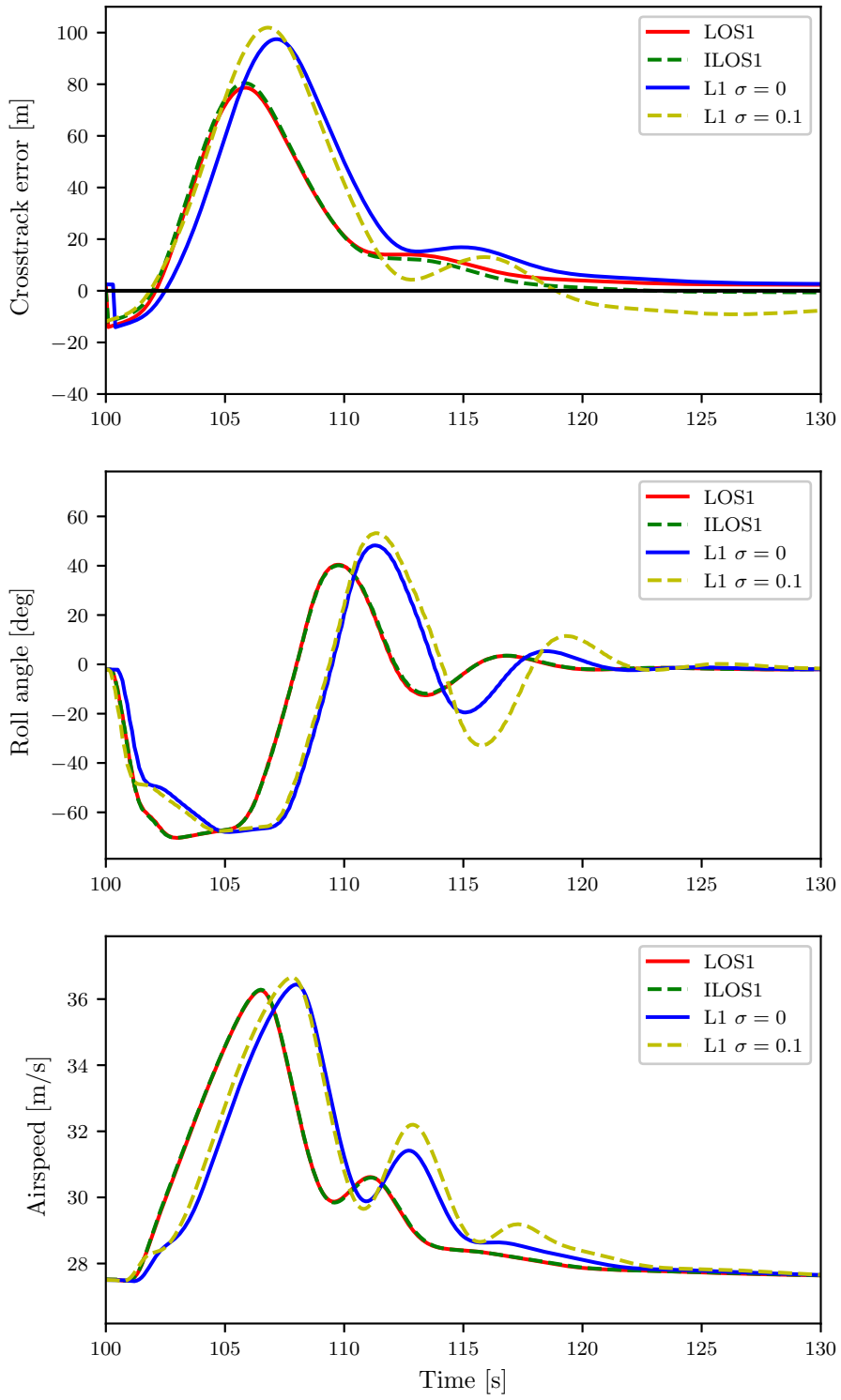

Figure 4.20: Crosstrack error, roll angle, and airspeed of between WP2 and WP3 using path 1 with steady wind

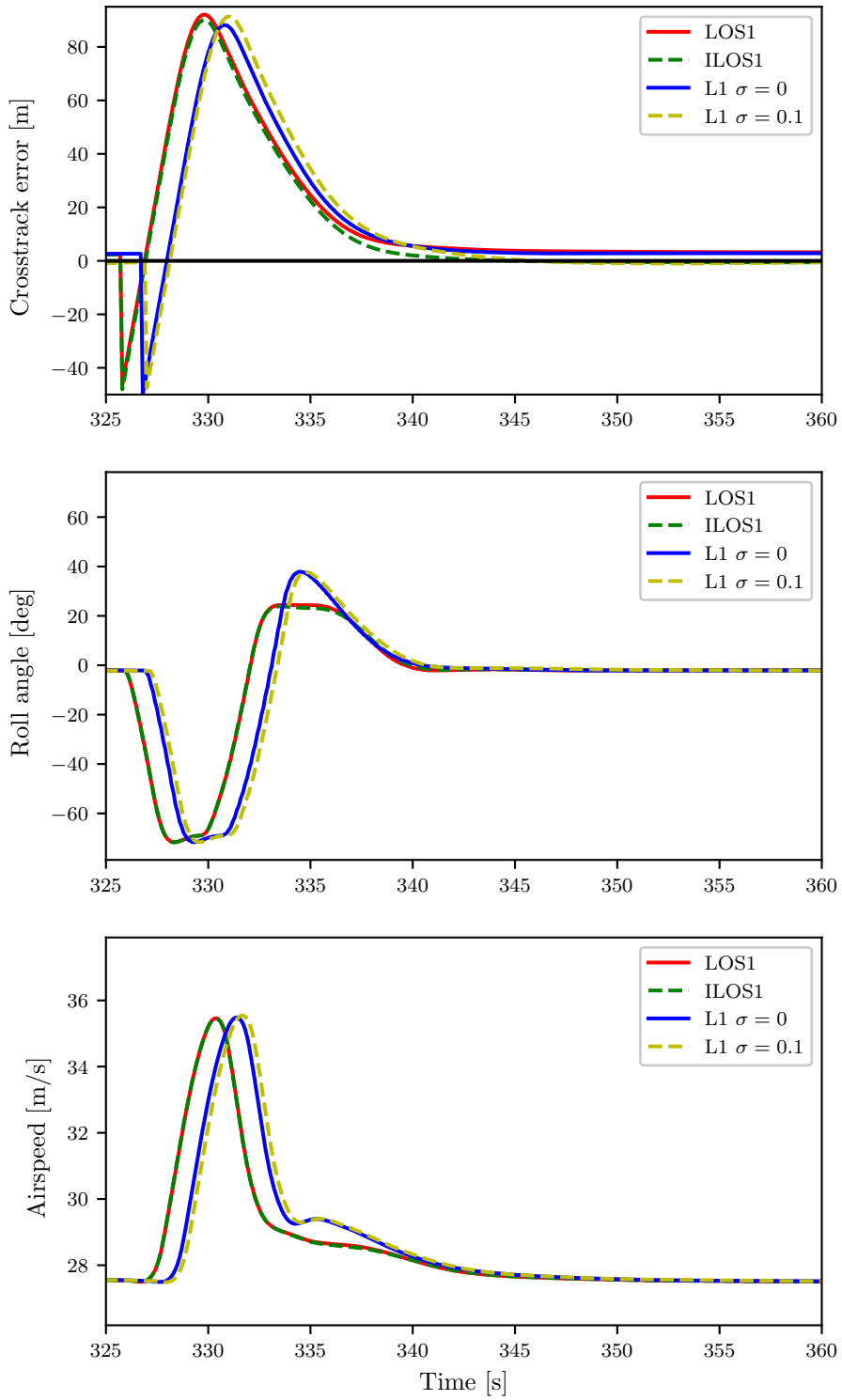

Figure 4.21: Crosstrack error, roll angle, and airspeed of between WP6 and WP7 using path 1 with steady wind

Chapter 5

Discussion

There seems to be nothing gained from including AOA and SSA in the guidance system. The performance of LOS1, LOS2, and LOS3 is nearly identical for both climbing and level flight for good AOA and SSA estimates. When the estimates are biased, the performance worsens. Furthermore, they are known to be hard to estimate in the real world because the wind is stochastic. As the results from Section 4.2 support the validity of Assumption A6, it can therefore be argued that one can do without including potentially biased or noisy AOA and SSA estimates in the coordinated-turn LOS guidance law.

The same argument can be made for including the pitch and flight path angles in coordinated-turn LOS. LOS1 does not seem to hold any advantage over LOS2 in terms of performance. Furthermore, in Section 4.3 it was seen that biased pitch angle estimates can give steady-state offset. One can therefore again argue that including these estimates, instead of assuming them to be zero, risks worsening performance without much to gain. A possible objection would be that a more dynamic flight model following a steeper path could have better use of the estimates. This could also be the case for LOS3 and LOS4 with AOA and SSA estimates. However, a more dynamic path following could put the coordinated turn assumptions at risk, likely Assumptions A4-A6, and might make coordinated-turn LOS less applicable for that situation.

Unfortunately, including the heading angle can not be avoided for LOS guidance as that is also known to be hard to estimate with magnetometers for small UAVs. The results in Section 4.3 showed that heading bias gave progressively more cross-track error oscillations. However, even with considerable bias in measurements, the coordinated-turn-inspired LOS guidance laws follow the path to some degree. This could be explained by the USGES property of the interconnected system of Equation (2.21) and Equation (2.39) shown in [2]. As stated in Section 2.2.1, USGES give strong robustness properties [20]. Note that the heading bias is usu-

ally not constant but will drift over time. Here it is kept constant to allow for more control over the variables of the simulation.

If biased measurements cause steady-state cross-track error, as for pitch bias, it could be removed with integral action. The various integral LOS guidance schemes in Section 4.4 showed that integral effect gave path convergence but more overshoot. Having the integral state grow on either cross-track or course error seemed like valid solutions. ILOS1 had less overshoot than CILOS2 and CILOS4, as the scaling factor was developed for cross-track error in [8]. However, applying the scaling factor reduced the cross-track error overshoot contribution from the integral state for all integral LOS variants, demonstrating the scaling factor's utility.

The L1 guidance law had a little more overshoot than coordinated-turn LOS in some situations, but in terms of robustness, it is clear that L1 has a decisive advantage over coordinated-turn LOS. It depends on fewer estimates: no heading, course, pitch, FPA, SSA, or SSB. Only position and velocity which are less prone to error with a good GNSS.

Chapter 6

Conclusion

Guidance for fixed-wing UAVs has been investigated in simulations with different variants of coordinated-turn-inspired LOS. The guidance law was derived with non-zero AOA and SSB to examine the assumptions behind the coordinated turn relation. The robustness of the coordinated-turn-inspired LOS was studied with biased AOA, SSB, pitch, and heading angle estimates. The simulation results suggested that there was not much to gain in terms of performance by including more estimates and aerodynamics in the guidance system. On the other hand, there was a risk of worsening it with faulty estimates. However, the aircraft was still able to follow the path with some bias, likely due to the robustness properties of the coordinated-turn-LOS guidance law.

A mathematical analysis of coordinated-turn-inspired integral LOS was done where UGAS and ULES were shown, resulting in global κ-exponential stability. Additionally, it was tested in simulations along with other integral LOS variants. They were demonstrated to remove the steady-state error but increase overshoot. The selection of the integral gain was deemed important, especially if the growth of the integral state was not scaled.

In the end, the coordinated-turn-inspired LOS guidance laws were compared to the L1 guidance law. The performance was shown to be quite similar, except for a little more overshoot in certain situations for the L1 guidance law. However, it is a more robust choice, as it depends on far fewer estimates.

Future work would include testing with a more dynamic flight model, where more aerodynamics in the guidance law could play a larger role, possibly with atmospheric disturbances. New integral effect schemes could also be tested, perhaps with a damping term to the LOS law. With atmospheric disturbances, extended-state observer LOS could be an interesting approach.

Bibliography

[1] H. A. Hansen, 'Guidance for a fixed-wing uav under large environmental forces,' *Unpublished. Specialization project - TTK4550*, 2023.

[2] K. Gryte, 'Precision control of fixed-wing uav and robust navigation in gnss-denied environments,' *Doctoral theses at NTNU, 2020:198*, 2020.

[3] Aviant. 'About aviant.' (2022), [Online]. Available: https://www.aviant.no/about (visited on 05/01/2023).

[4] A. M. Lekkas and T. I. Fossen, 'A time-varying lookahead distance guidance law for path following,' *IFAC Proceedings Volumes, Elsevier*, vol. 45, pp. 398–403, 2012.

[5] A. M. Lekkas and T. I. Fossen, 'Line-of-sight guidance for path following of marine vehicles,' *Advanced in marine robotics, San Francisco, CA, USA: Academic*, pp. 63–92, 2013.

[6] A. M. Lekkas and T. I. Fossen, 'Minimization of cross-track and along-track errors for path tracking of marine underactuated vehicles,' *Control Conference (ECC), 2014 European*, pp. 3004–3010, 2014.

[7] B. Breivik and T. I. Fossen, 'Applying missile guidance concepts to motion control of marine craft,' *IFAC Proceedings Volumes*, vol. 40, no. 17, pp. 349–354, 2007, 7th IFAC Conference on Control Applications in Marine Systems, ISSN: 1474-6670. DOI: https://doi.org/10.3182/20070919-3-HR-3904.00061. [Online]. Available: https://www.sciencedirect.com/science/article/pii/S1474667015321200.

[8] E. Borhaug, A. Pavlov and K. Y. Pettersen, 'Integral los control for path following of underactuated marine surface vessels in the presence of constant ocean currents,' *2008 47th IEEE Conference on Decision and Control*, pp. 4984–4991, 2008. DOI: 10.1109/CDC.2008.4739352.

[9] A. M. Lekkas and T. I. Fossen, 'Integral los path following for curved paths based on a monotone cubic hermite spline parametrization,' *IEEE Transactions on Control Systems Technology, IEEE*, vol. 45, pp. 398–403, 2014.

[10] T. I. Fossen and A. M. Lekkas, 'Direct and indirect adaptive integral line-of-sight path-following controllers for marine craft exposed to ocean currents,' *International Journal of Adaptive Control and Signal Processing*, vol. 31, no. 4, pp. 445–463, 2017. DOI: https://doi.org/10.1002/acs.2550. eprint: https://onlinelibrary.wiley.com/doi/pdf/10.1002/acs.2550. [Online]. Available: https://onlinelibrary.wiley.com/doi/abs/10.1002/acs.2550.

[11] N. Gu, D. Wang, Z. Peng, J. Wang and Q.-L. Han, 'Advances in line-of-sight guidance for path following of autonomous marine vehicles: An overview,' *IEEE Transactions on Systems, Man, and Cybernetics: Systems*, vol. 53, no. 1, pp. 12–28, 2023. DOI: 10.1109/TSMC.2022.3162862.

[12] L. Liu, D. Wang and Z. Peng, 'Eso-based line-of-sight guidance law for path following of underactuated marine surface vehicles with exact sideslip compensation,' *IEEE Journal of Oceanic Engineering*, vol. 42, no. 2, pp. 477–487, 2017. DOI: 10.1109/JOE.2016.2569218.

[13] M. Li, C. Guo and H. Yu, 'Extended state observer-based integral line-of-sight guidance law for path following of underactuated unmanned surface vehicles with uncertainties and ocean currents,' *International Journal of Advanced Robotic Systems*, vol. 18, no. 3, p. 17 298 814 211 011 035, 2021.

[14] S. Park, J. Deyst and J. P. How, 'A new nonlinear guidance logic for trajectory tracking,' *Proceedings of the AIAA Guidance, Navigation and Control Conference,*, 2004.

[15] S. Park, J. Deyst and J. P. How, 'Performance and lyapunov stability of a nonlinear path following guidance method,' *Journal of Guidance, Control, and Dynamics*, vol. 30, pp. 1718–1728, 2007.

[16] R. Curry, M. Lizarraga, B. Mairs and G. H. Elkaim, 'L2, an improved line of sight guidance law for uavs,' *American Control Conference (ACC)*, 2013.

[17] R. Beard and T. McLain, *Small Unmanned Aircraft: Theory and Practice*. Princeton University Press, 2012.

[18] R. F. Stengel, *Flight dynamics*. Princeton university press, 2004.

[19] T. I. Fossen, *Handbook of Marine Craft Hydrodynamics and Motion Control*. John Wiley and Sons, Ltd, 2011, ch. 10, pp. 241–284.

[20] T. I. Fossen and K. Y. Pettersen, 'On uniform semiglobal exponential stability (usges) of proportional line-of-sight guidance laws,' *Automatica*, vol. 50, no. 11, pp. 2912–2917, 2014.

[21] O. J. Sordalen and O. Egeland, 'Exponential stabilization of nonholonomic chained systems,' *IEEE transactions on automatic control*, vol. 40, no. 1, pp. 35–49, 1995.

[22] A. A. J. Lefeber, *Tracking control of nonlinear mechanical systems*. Universiteit Twente Enschede, 2000.

[23] M. Breivik and T. Fossen, 'Guidance laws for autonomous underwater vehicles,' *Underwater Vehicles*, Jan. 2009. DOI: 10.5772/6696.

[24] C. M. Bishop, 'Integral guidance for ballistic missiles,' *1976 IEEE Conference on Decision and Control including the 15th Symposium on Adaptive Processes*, pp. 1159–1163, 1976. DOI: 10.1109/CDC.1976.267661.

[25] M. Davidson, V. Bahl and K. Moore, 'Spatial integration for a nonlinear path tracking control law,' vol. 5, 4291–4296 vol.5, 2002. DOI: 10.1109/ACC.2002.1024607.

[26] W. Caharija, K. Y. Pettersen, M. Bibuli, P. Calado, E. Zereik, J. Braga, J. T. Gravdahl, A. J. Sørensen, M. Milovanović and G. Bruzzone, 'Integral line-of-sight guidance and control of underactuated marine vehicles: Theory, simulations, and experiments,' *IEEE Transactions on Control Systems Technology*, vol. 24, no. 5, pp. 1623–1642, 2016. DOI: 10.1109/TCST.2015.2504838.

[27] E. Kelasidi, P. Liljebäck, K. Y. Pettersen and J. T. Gravdahl, 'Integral line-of-sight guidance for path following control of underwater snake robots: Theory and experiments,' *IEEE Transactions on Robotics*, vol. 33, no. 3, pp. 610–628, 2017. DOI: 10.1109/TRO.2017.2651119.

[28] G. Zhang, J. Li, B. Li and X. Zhang, 'Improved integral los guidance and path-following control for an unmanned robot sailboat via the robust neural damping technique,' *The Journal of Navigation*, vol. 72, no. 6, pp. 1378–1398, 2019. DOI: 10.1017/S0373463319000353.

[29] R. Rout, R. Cui and Z. Han, 'Modified line-of-sight guidance law with adaptive neural network control of underactuated marine vehicles with state and input constraints,' *IEEE Transactions on Control Systems Technology*, vol. 28, no. 5, pp. 1902–1914, 2020. DOI: 10.1109/TCST.2020.2998798.

[30] R. Rout, R. Cui and W. Yan, 'Sideslip-compensated guidance-based adaptive neural control of marine surface vessels,' *IEEE Transactions on Cybernetics*, vol. 52, no. 5, pp. 2860–2871, 2022. DOI: 10.1109/TCYB.2020.3023162.

[31] H. K. Khalil, *Nonlinear systems*, 3rd ed. Prentice Hall, 2002.

[32] JSBSim-Team. 'Jsbsim v1.1.12.' (2022), [Online]. Available: https://github.com/JSBSim-Team/jsbsim/releases/tag/v1.1.12 (visited on 05/06/2023).

[33] Ardupilot. 'Ardupilot project.' (2023), [Online]. Available: https://github.com/ArduPilot/ardupilot/tree/Plane-4.3.3 (visited on 22/05/2023).

[34] T. A. Johansen, A. Cristofaro, K. Sørensen, J. M. Hansen and T. I. Fossen, 'On estimation of wind velocity, angle-of-attack and sideslip angle of small uavs using standard sensors,' pp. 510–519, 2015. DOI: 10.1109/ICUAS.2015.7152330.

[35] J. F. D. Model. 'Fgwinds class reference.' (2022), [Online]. Available: https://jsbsim-team.github.io/jsbsim/classJSBSim_1_1FGWinds.html#aad7ec783b7dd73f5ebfabec4c0ba535c (visited on 14/05/2023).

[36] J. C. Yeager, 'Implementation and testing of turbulence models for the f18-harv simulation,' Tech. Rep., 1998.

[37] 'Flying qualities of piloted airplanes,' MIL-F-8785C: Military Specification, Tech. Rep., 1980.

[38] ArduPilot. 'Planning a mission with waypoints and events.' (2023), [Online]. Available: `https://ardupilot.org/copter/docs/common-planning-a-mission-with-waypoints-and-events.html` (visited on 15/05/2023).

Appendix A

Additional Material

A.1 Path description

This section contains detailed descriptions of the paths used in the simulations. They are defined as a series of waypoints in an Ardupilot mission, described as usual in a .txt file [38].

A.1.1 Path 1

```
    QGC WPL 110
0 1 0 16 0 0 0 0 -35.3629380 149.1650850 650.000000 1
1 0 3 22 15.00000000 0.00000000 0.00000000 0.00000000 -35.35983300 149.16470300
41.030000 1
2 0 3 16 0.00000000 0.00000000 0.00000000 0.00000000 -35.35976990 149.16145210
100.000000 1
3 0 3 16 0.00000000 0.00000000 0.00000000 0.00000000 -35.36002370 149.14719340
100.000000 1
4 0 3 16 0.00000000 0.00000000 0.00000000 0.00000000 -35.36245600 149.16214940
100.000000 1
5 0 3 16 0.00000000 0.00000000 0.00000000 0.00000000 -35.36245600 149.14457560
100.000000 1
6 0 3 16 0.00000000 0.00000000 0.00000000 0.00000000 -35.35657620 149.14406060
100.000000 1
7 0 3 16 0.00000000 0.00000000 0.00000000 0.00000000 -35.35643620 149.15760040
100.000000 1
8 0 3 16 0.00000000 0.00000000 0.00000000 0.00000000 -35.34887580 149.15794370
100.000000 1
9 0 3 16 0.00000000 0.00000000 0.00000000 0.00000000 -35.35927200 149.16375700
100.000000 1
10 0 3 177 2.00000000 -1.00000000 0.00000000 0.00000000 0.00000000 0.00000000
0.000000 1
11 0 3 16 0.00000000 0.00000000 0.00000000 0.00000000 -35.35927200 149.16375700
100.000000 1
```

A.1.2 Path 2

```
    QGC WPL 110
0 1 0 16 0 0 0 0 -35.3629380 149.1650850 650.000000 1
1 0 3 22 15.00000000 0.00000000 0.00000000 0.00000000 -35.35983300 149.16470300
41.030000 1
2 0 3 16 0.00000000 0.00000000 0.00000000 0.00000000 -35.35976990 149.16145210
100.000000 1
3 0 3 16 0.00000000 0.00000000 0.00000000 0.00000000 -35.35967370 149.14708610
400.000000 1
4 0 3 16 0.00000000 0.00000000 0.00000000 0.00000000 -35.36245600 149.16214940
100.000000 1
5 0 3 16 0.00000000 0.00000000 0.00000000 0.00000000 -35.36245600 149.14457560
400.000000 1
6 0 3 16 0.00000000 0.00000000 0.00000000 0.00000000 -35.35657620 149.14406060
100.000000 1
7 0 3 16 0.00000000 0.00000000 0.00000000 0.00000000 -35.35643620 149.15760040
200.000000 1
8 0 3 16 0.00000000 0.00000000 0.00000000 0.00000000 -35.34887580 149.15794370
400.000000 1
9 0 3 16 0.00000000 0.00000000 0.00000000 0.00000000 -35.35927200 149.16375700
100.000000 1
10 0 3 177 2.00000000 -1.00000000 0.00000000 0.00000000 0.00000000 0.00000000
0.000000 1
11 0 3 16 0.00000000 0.00000000 0.00000000 0.00000000 -35.35927200 149.16375700
100.000000 1
```

A.1.3 Path 3

```
    QGC WPL 110
0 1 0 16 0 0 0 0 -35.3629380 149.1650850 650.000000 1
1 0 3 22 15.00000000 0.00000000 0.00000000 0.00000000 -35.35983300 149.16470300
41.030000 1
2 0 3 16 0.00000000 0.00000000 0.00000000 0.00000000 -35.35976990 149.16145210
100.000000 1
3 0 3 16 0.00000000 0.00000000 0.00000000 0.00000000 -35.35967370 149.14708610
400.000000 1
4 0 3 16 0.00000000 0.00000000 0.00000000 0.00000000 -35.36245600 149.16214940
100.000000 1
5 0 3 16 0.00000000 0.00000000 0.00000000 0.00000000 -35.36245600 149.14457560
400.000000 1
6 0 3 16 0.00000000 0.00000000 0.00000000 0.00000000 -35.33175720 149.14498330
100.000000 1
7 0 3 16 0.00000000 0.00000000 0.00000000 0.00000000 -35.35643620 149.15760040
200.000000 1
8 0 3 16 0.00000000 0.00000000 0.00000000 0.00000000 -35.33105690 149.15845870
400.000000 1
9 0 3 16 0.00000000 0.00000000 0.00000000 0.00000000 -35.35927200 149.16375700
100.000000 1
10 0 3 177 2.00000000 -1.00000000 0.00000000 0.00000000 0.00000000 0.00000000
0.000000 1
11 0 3 16 0.00000000 0.00000000 0.00000000 0.00000000 -35.35927200 149.16375700
100.000000 1
```

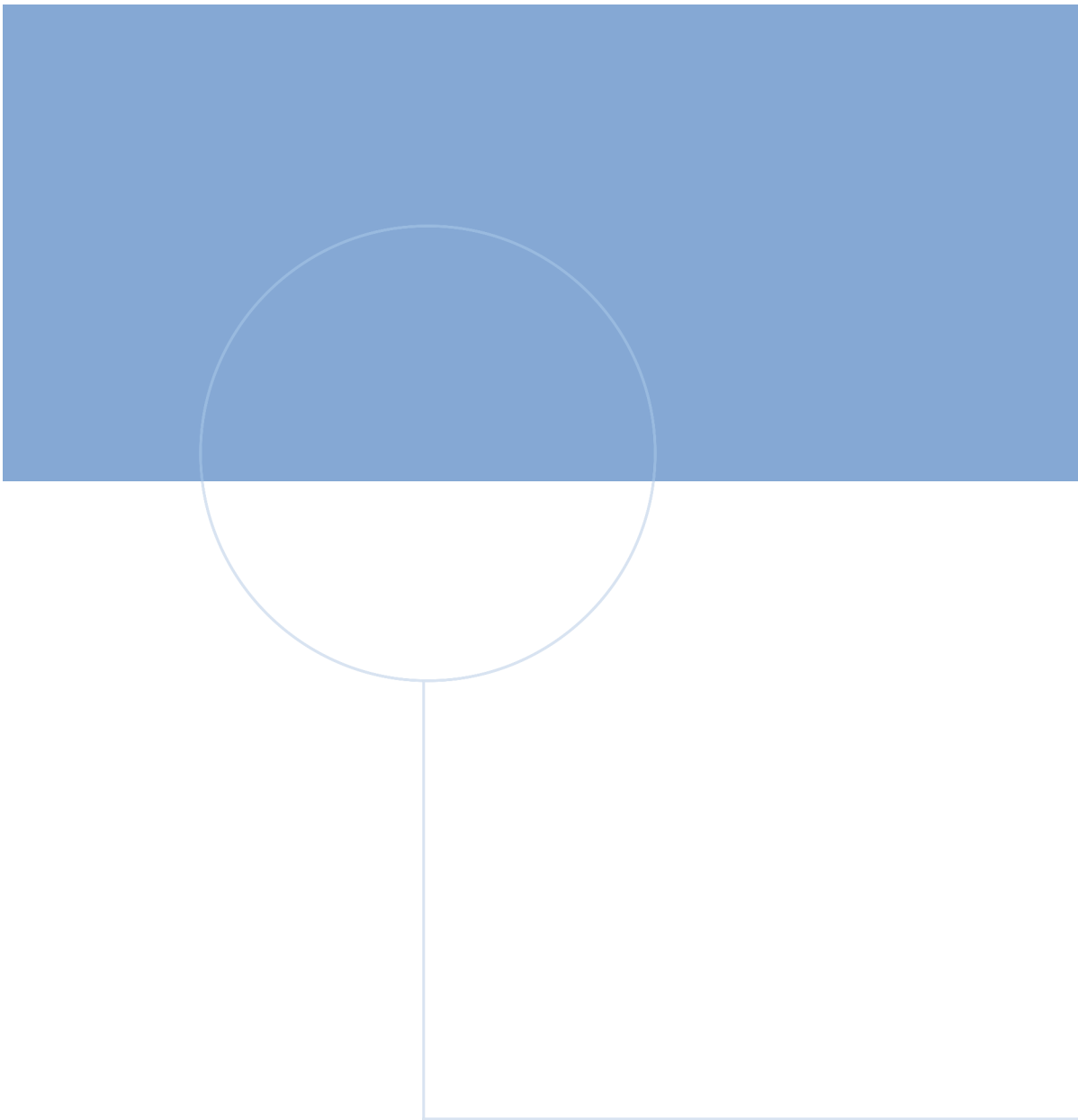

NTNU

Norwegian University of
Science and Technology